

1 Estimating Radiative Forcing Efficiency of Dust Aerosol 2 Based on Direct Satellite Observations: Case Studies over 3 the Sahara Desert and Taklimakan Desert

4 Lin Tian^{1,2,3}, Lin Chen³, Peng Zhang³, Lei Bi⁴

5 ¹Nanjing University of Information Science & Technology, Nanjing, China.

6 ²Chinese Academy of Meteorological Sciences, Beijing, China.

7 ³National Satellite Meteorological Center, China Meteorological Administration, Beijing, China.

8 ⁴Department of Atmospheric Sciences, School of Earth Sciences, Zhejiang University, Hangzhou,
9 China.

10 *Correspondence to:* Peng Zhang (zhangp@cma.gov.cn) & Lin Chen (chenlin@cma.gov.cn)

11 **Abstract.** The direct radiative forcing efficiency of the dust aerosol ($DRFE_{\text{dust}}$) is an important indicator
12 to measure the climate effect of the dust. The $DRFE_{\text{dust}}$ is determined by the microphysical properties
13 of the dust, which vary with the dust source regions. However, there are only sparse in-situ
14 measurements of them, such as the distribution of the dust aerosol particle size and the complex
15 refractive index in the main dust source regions. Furthermore, recent studies have shown that the
16 non-spherical effect of the dust particle is not negligible. The $DRFE_{\text{dust}}$ is often evaluated by estimating
17 given microphysical properties of the dust aerosols in the radiative transfer model (RTM). However,
18 considerable uncertainties exist due to the complex and variable dust properties, including the complex
19 refractive index and the shape of the dust. The $DRFE_{\text{dust}}$ over the Taklimakan Desert and the Sahara
20 Desert is derived from the satellite observations in this paper. The advantage of the proposed
21 satellite-based method is that there is no need to consider the microphysical properties of the dust
22 aerosols in estimating the $DRFE_{\text{dust}}$. For comparison, the observed $DRFE_{\text{dust}}$ is compared with that
23 simulated by the RTM. The differences in the dust microphysical properties in these two regions and
24 their impacts on $DRFE_{\text{dust}}$ are analyzed.

25 The $DRFE_{\text{dust}}$ derived from the satellite observation is $-39.6 \pm 10.0 \text{ Wm}^{-2}\tau^{-1}$ in March 2019 over
26 Tamanrasset in the Sahara Desert and $-48.6 \pm 13.7 \text{ Wm}^{-2}\tau^{-1}$ in April 2019 over Kashi in the
27 Taklimakan Desert. According to the analyses of their microphysical properties and optical properties,
28 the dust aerosols from the Taklimakan Desert (Kashi) scatter strongly. The RTM simulated results
29 (-41.5 to $-47.4 \text{ Wm}^{-2}\tau^{-1}$ over Kashi and -32.2 to $-44.3 \text{ Wm}^{-2}\tau^{-1}$ over Tamanrasset) are in good
30 agreement with the results estimated by satellite observations. According to previous studies, the

31 results in this paper are proved to be reasonable and reliable. The results also show that the
32 microphysical properties of the dust can significantly influence the $DRFE_{dust}$. The satellite-derived
33 results can represent the influence of the dust microphysical properties on the $DRFE_{dust}$, which can also
34 validate the direct radiative effect of the dust aerosol and the $DRFE_{dust}$ derived from numerical model
35 more directly.

36 **1 Introduction**

37 Dust aerosols are considered to be one of the major components of the tropospheric aerosols
38 (Huneeus et al., 2012;Textor et al., 2007). The dust aerosols affect the radiation balance of the
39 earth-atmosphere system by scattering and absorbing solar radiation directly (Miller et al.,
40 2014;Satheesh, 2002). Estimating the direct radiation effect of the dust aerosol (DRE_{dust}) is crucial for
41 estimating climate forcing. The scattering of the dust influences the radiation in the shortwave (SW)
42 spectrum at the top of atmosphere (TOA), which causes stronger SW DRE_{dust} over dust source regions
43 (Slingo et al., 2006). Therefore, the evaluation of SW DRE_{dust} is important for climate modeling.

44 The variabilities of the mineral dust composition from soils in different source regions cause the
45 differences in dust microphysical properties (e.g., refractive index, size, and particle shapes). The
46 Direct Radiative Forcing Efficiency of the dust aerosol ($DRFE_{dust}$) is defined to quantify the dust
47 radiative effect (Anderson et al., 2005;Satheesh and Ramanathan, 2000). The $DRFE_{dust}$ represents the
48 DRE_{dust} of per unit aerosol optical depth (AOD), which means the efficiency of the dust aerosol that
49 affects the net radiative flux of solar radiation. The $DRFE_{dust}$ is largely determined by the optical
50 properties of the dust aerosols (Shi et al., 2005), which are strictly controlled by the microphysical
51 properties of the particles (Di Biagio et al., 2014b;Di Biagio et al., 2017;Di Biagio et al., 2014a;Zhang
52 et al., 2006). Therefore, the $DRFE_{dust}$ is different concerning the dust aerosols from different source
53 regions (Tanré et al., 2001;Che et al., 2012). Without considering the influence of the aerosol loading
54 on the DRE_{dust} , the $DRFE_{dust}$ has unique advantages in evaluating the differences of dust microphysical
55 properties and their impacts on the DRE_{dust} from different dust source regions (García et al., 2008).

56 The $DRFE_{dust}$ is often estimated by the General Circulation Model (GCM) and the Radiative
57 Transfer Model (RTM). Many studies have simulated the SW $DRFE_{dust}$ in different regions
58 (Valenzuela et al., 2012;Che et al., 2009;Bi et al., 2014). However, there are sparse in-situ

59 measurements of the dust microphysical properties in the main source regions. The large spatial
60 variability of aerosols and the lack of an adequate database on their properties make DRE_{dust} and
61 $DRFE_{dust}$ much very difficult to be estimated (Satheesh and Srinivasan, 2006). To date, climate models
62 generally use temporal and spatial constant values to represent the dust microphysical properties (Di
63 Biagio et al., 2017; Di Biagio et al., 2014a; Bi et al., 2020). This may cause uncertainties in calculating
64 the dust radiative effect. Moreover, the shape of the dust particle in the model needs to be assumed.
65 Therefore, there are large uncertainties in estimating the $DRFE_{dust}$ with few measurements of the dust
66 microphysical properties from different source regions (Bi et al., 2020; Colarco et al., 2014; Zhao et al.,
67 2013).

68 Satellite observations can be used in estimating the $DRFE_{dust}$ because satellites can directly
69 observe the radiation budget of the earth at the TOA (Wielicki et al., 1998; Satheesh and Ramanathan,
70 2000), and the remote-sensing technique for the AOD has been developed (Remer et al., 2005; Hsu et
71 al., 2004). In the previous study, we developed a satellite-based method to estimate the $DRFE_{dust}$ over
72 land without any assumptions of the microphysical properties of dust aerosols (Tian et al., 2019). In
73 previous researches, performances of the models in simulating the dust radiative effect have been
74 indirectly validated by comparing the observations of the AOD, the single scattering albedo (SSA), the
75 distribution of the particle size, and the extinction profile of the aerosols with the simulated ones (Zhao et
76 al. 2010; Chen et al. 2014). Therefore, the satellite-based method provides a direct way to validate the
77 DRE_{dust} and the $DRFE_{dust}$.

78 The Sahara Desert and the Taklimakan Desert are the main dust source regions, which influence
79 many areas (Li et al., 2020; Mikami et al., 2006; Mbourou et al., 1997; Huang et al., 2014). Previous
80 studies also estimated the $DRFE_{dust}$ in the Sahara Desert and the Taklimakan Desert (Li et al., 2020; Li
81 et al., 2004; Garc ía et al., 2012; Xia and Zong, 2009). Garc ía et al. (2012) evaluated the $DRFE_{dust}$ in the
82 Sahara Desert based on the Global Atmospheric Model (GAME) and the AERONET retrievals. Li et al.
83 (2004) estimated $DRFE_{dust}$ in the Sahara Desert based on the satellite data and the SBDART model. For
84 the Taklimakan Desert, Li et al. (2020) estimated the instantaneous SW $DRFE_{dust}$ based on the RTM
85 and ground-based measurements of dust properties. Xia and Zong (2009) used both the satellite data
86 and the SBDART model to represent the instantaneous SW $DRFE_{dust}$ at the TOA (Xia and Zong, 2009).
87 The $DRFE_{dust}$ varies in these studies, and the differences may come from the different research
88 conditions and the difference of dust aerosol microphysical properties in the Sahara Desert and the

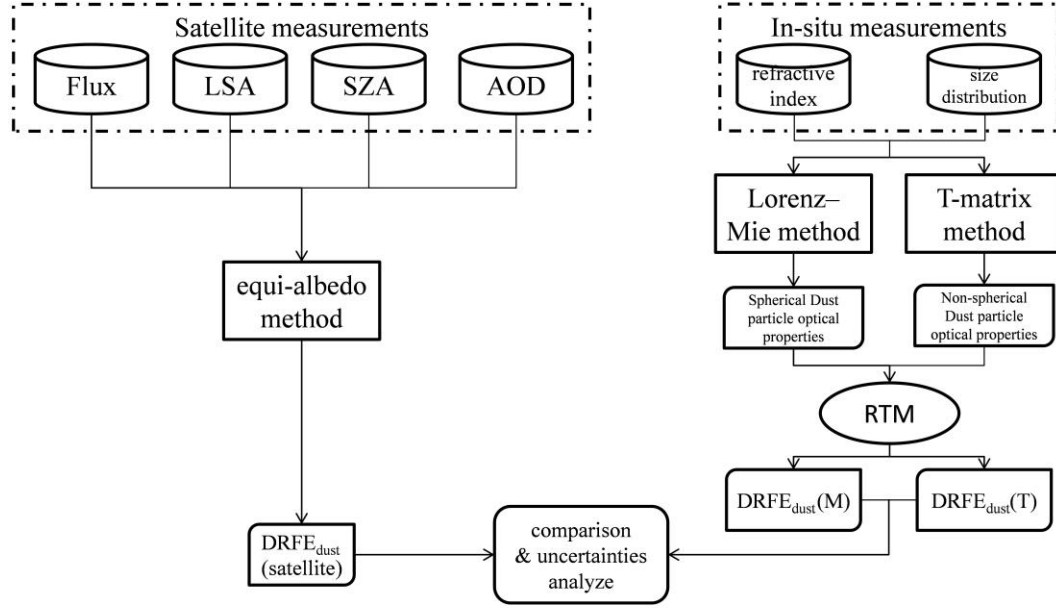
89 Taklimakan Desert. Thus, the assessment on the SW $DRFE_{dust}$ and dust microphysical properties over
90 the Sahara Desert and the Taklimakan Desert is meaningful to evaluate regional and global climate
91 changes.

92 In this paper, the $DRFE_{dust}$ at the TOA in dust storms over Tamanrasset in the Sahara Desert and
93 Kashi in the Taklimakan Desert are evaluated based on satellite observations and the RTM, separately.
94 With the comparison of the dust microphysical properties and the $DRFE_{dust}$ at the TOA in these two
95 regions, the differences of the dust microphysical properties are analyzed. Meanwhile, the influences of
96 the dust microphysical properties on the $DRFE_{dust}$ at the TOA are investigated in this paper. The need
97 for accurate information on the dust microphysical properties and dust sources for simulating the
98 $DRFE_{dust}$ is emphasized, and the advantage of the satellite-based method in estimating the $DRFE_{dust}$ is
99 revealed.

100 **2 Methodology and data**

101 In the previous study (Tian et al., 2019), the equi-albedo method has been proposed to estimate the
102 DRE_{dust} and the $DRFE_{dust}$ at the TOA over land based on satellite measurements directly. This method
103 bases on the assumption that the SW radiative fluxes at the TOA of the clear sky (F_{clr}) are equal over the
104 regions with similar land surface albedo (LSA) and solar zenith angle (SZA). Following this method, we
105 estimated the $DRFE_{dust}$ based on the AOD and the SW radiative flux product from the same satellite
106 platform.

107 Moreover, the $DRFE_{dust}$ in the RTM with dust aerosol microphysical properties is also evaluated.
108 Based on the comparison between the $DRFE_{dust}$ results from the two methods, the differences in the dust
109 microphysical properties over the Taklimakan Desert and the Sahara Desert are analyzed, and the
110 differences in the $DRFE_{dust}$ at the TOA are also discussed. The processing steps are shown in Fig. 1.



Flux: Radiative Flux observed by CERES;

LSA: Land Surface Albedo;

SZA: Solar zenith Angle;

AOD: Aerosol Optical Depth;

DRFE_{dust}(satellite): DRFE_{dust} estimated from satellite measurements

DRFE_{dust}(M): DRFE_{dust} simulated from Lorenz-Mie method and RTM;

DRFE_{dust}(T): DRFE_{dust} simulated from T-matrix method and RTM;

111

112 **Figure 1: Processing flow chart of this paper.**

113 2.1 Methodology

114 2.1.1 The equi-albedo method

115 Previous studies have shown that F_{clr} is significantly influenced by the LSA and the SZA at the
 116 TOA (Di Biagio et al., 2012; Tegen et al., 2010). It is hard to assess the SW DRE_{dust} and the $DRFE_{dust}$
 117 over land derived from satellite observations due to the large dynamic range of the LSA (Satheesh,
 118 2002). In the previous study (Tian et al., 2019), we proposed an equi-albedo method to minimize the
 119 influence of the inhomogeneous LSA and SZA and directly derived the DRE_{dust} and the $DRFE_{dust}$ over
 120 land from satellite observations based on the assumption that the F_{clr} is equal over the regions with
 121 similar LSA and SZA.

122 DRE_{dust} is defined as the upward radiative flux difference between clear (F_{clr}) and dust loading
 123 (F_{dust}) conditions (Garrett and Zhao, 2006; Christopher et al., 2000; Ramanathan et al., 1989).

$$124 \quad DRE_{dust} = F_{clr} - F_{dust} \quad (1).$$

125 F_{dust} is the shortwave radiative flux at the TOA under the cloud-free and dust aerosol loading
 126 conditions which is obtained directly from the Clouds and the Earth's Radiant Energy System (CERES).

127 F_{clr} is the shortwave flux over the same region without aerosol. F_{clr} cannot be observed directly, and
128 the estimating of F_{clr} must be on the basis of some realistic assumptions.

129 The equi-albedo method bases on the assumption that the upward SW radiative flux at the TOA of
130 the clear sky (F_{clr}) are equal over the regions with similar land surface albedo (LSA) and solar zenith
131 angle (SZA). In the equi-albedo method we set the cloud-free pixels with AOD smaller than 0.1 as the
132 clear-sky pixels (Tian et al., 2019). Therefore, it can be considered to be in the same condition when
133 the difference between LSA is less than 0.01, and the difference between SZA is less than 0.2° . This
134 keeps good consistency of F_{clr} between clear and dust storm area, and ensures that enough pixels
135 could match the condition (Tian et al., 2019). Based on the assumption, the F_{clr} is estimated, and then
136 DRE_{dust} can be derived following Eq. (1). According to the definition of $DRFE_{\text{dust}}$, it represents the net
137 flux of solar radiation perturbed by per unit dust AOD. Therefore, $DRFE_{\text{dust}}$ can be expressed as:

$$138 \quad DRFE_{\text{dust}} = DRE_{\text{dust}}/\tau_{\text{dust}} \quad (2)$$

139 where τ_{dust} is the AOD of dust aerosols, and τ_{dust} comes from the MODIS aerosol product.
140 Thus, $DRFE_{\text{dust}}$ is estimated based on the AOD and the SW radiative flux product from the same
141 satellite platform.

142 In the previous study (Tian et al., 2019), we have estimated the DRE_{dust} and the $DRFE_{\text{dust}}$ of two
143 dust storms in the Taklimakan Desert. The results were compared with the DRE_{dust} and the $DRFE_{\text{dust}}$
144 simulated by the RTM. The results indicated that the method is effective in estimating the SW $DRFE_{\text{dust}}$
145 over land. The microphysical properties of dust aerosols significantly influence on the DRE_{dust} and the
146 $DRFE_{\text{dust}}$ (Che et al., 2012; Li et al., 2018). The different microphysical properties of dust aerosols in
147 various dust source regions cause uncertainties in estimating the SW DRE_{dust} and $DRFE_{\text{dust}}$. Thus, the
148 equi-albedo method is used to estimate the SW $DRFE_{\text{dust}}$ directly using satellite observations in this
149 study. Based on the comparison of the $DRFE_{\text{dust}}$ in the Taklimakan Desert and the Sahara Desert, the
150 differences of dust microphysical properties in these two regions are analyzed and the influences of the
151 dust microphysical properties on estimating the $DRFE_{\text{dust}}$ are tested.

152 **2.1.2 Calculating method of dust optical properties**

153 Dust aerosols are often assumed as spherical particles in the GCM and the RTM (Wang et al.,
154 2013; Gao and Anderson, 2001). The Lorenz-Mie theory is used to calculate the optical properties of the
155 dust particles (Gouesbet and Gréhan, 2011). However, observations and researches have shown that

156 most dust aerosols are non-spherical in nature (Nakajima et al., 1989;Okada et al., 2001). Previous
157 researches also suggested that assuming particles as spherical or non-spherical has significant impacts
158 on calculating the dust optical properties (Kalashnikova and Sokolik, 2004;Borghese et al., 2007).
159 Therefore, the optical properties of dust aerosols are calculated using both the spherical and the
160 ellipsoidal methods for comparison to analyze the uncertainties caused by the assumption of dust
161 shapes in estimating the $DRFE_{dust}$ in this study.

162 To make it more accurate, the light scattering properties of spherical particles are generally
163 calculated based on the Mie and Lorenz theory (Mishchenko and Travis, 2008). Among several
164 methods for computing optical properties of non-spherical particles, the T-matrix method has been
165 extensively developed to many versions for various applications (Chylek et al., 1977;Mishchenko et al.,
166 1996). These versions of the available T-matrix codes are accessed from the National Aeronautics and
167 Space Administration (NASA) Goddard Institute for Space Studies (GISS) group. The T-matrix codes
168 are accessed from the National Aeronautics and Space Administration (NASA) Goddard Institute for
169 Space Studies (GISS) group (https://www.giss.nasa.gov/staff/mmishchenko/t_matrix.html). The codes
170 are directly applicable to spheroids and finite circular cylinders, and spheroids are formed by rotating
171 an ellipse about its minor (oblate spheroid) or major (prolate spheroid) axis (Mishchenko and Travis,
172 1998). The shape and size of a spheroid can be conveniently specified by the aspect ratio. The aspect
173 ratio is greater than 1 for oblate spheroids, smaller than 1 for prolate spheroids, and equal to 1 for
174 spheres. Therefore, Mie scattering method can be regarded as a special case of the T-matrix method. In
175 this study in order to calculate the dust aerosol optical properties, the dust particles are assumed to be a
176 sphere (aspect ratio equals to 1) and an ellipsoid (aspect ratio equals to 0.8). Furthermore, the
177 differences of aerosol optical properties between different shape assumptions are discussed.

178 **2.1.3 RTM**

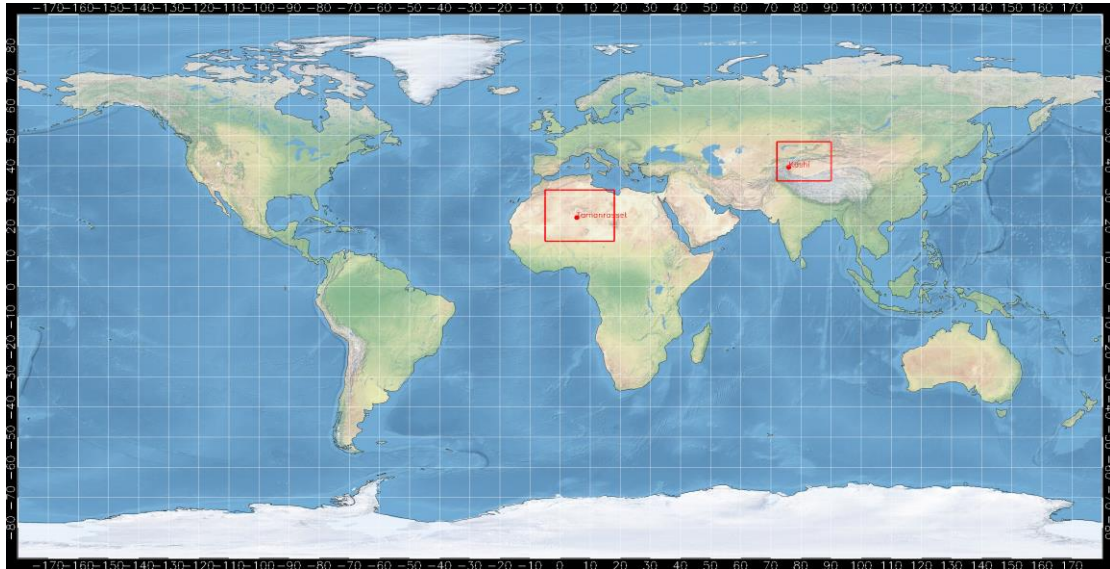
179 Santa Barbara Disort DISORT Atmospheric Radiative Transfer (SBDART) is an RTM that
180 calculates the plane-parallel radiative transfer of the earth-atmosphere system (Ricchiazzi et al., 1998a).
181 The broadband radiative flux at the TOA and the surface in clear-sky and dusty conditions can be
182 obtained. It is conducive to analyzing the radiative transfer theory in satellite remote sensing and
183 atmospheric energy budget studies. Furthermore, the model can flexibly set up aerosol properties,
184 which is well suited to calculate the radiative effect of different types of aerosols. The SBDART model

185 has been widely used in estimating the $DRFE_{dust}$ due to its design (Chen et al., 2011;Li et al.,
186 2020;Iftikhar et al., 2018).

187 In this paper, the dust aerosol optical properties (the SSA and the ASYmmetry parameter,
188 abbreviated as ASY) are calculated using spherical and non-spherical methods. The Aerosol Robotic
189 Network (AERONET) retrieves the physical properties of aerosols including volume size distribution
190 and the complex refractive index, and optical properties including the SSA and the ASY (Dubovik and
191 King, 2000;Dubovik et al., 2006). The LSA from Moderate Resolution Imaging Spectroradiometer
192 (MODIS) surface albedo product, and the default atmospheric profile of SBDART (MID-LATITUDE
193 WINTER) are used as the input parameters for the SBDART model in simulating the $DRFE_{dust}$. In
194 SBDART model, users can define the aerosol spectral dependence by few wavelengths points, and the
195 aerosol optical properties are extrapolated to other wavelengths by a power law (Ricchiuzzi et al.,
196 1998b). Therefore, aerosol properties measured at four wavelengths are extrapolated so that flux
197 calculations can be made in any desired wavelength across the shortwave spectrum (McComiskey et al.,
198 2021). Therefore, the DRE_{dust} changing with the AOD due to both dust aerosol microphysical
199 properties (including the complex refractive index and the distribution of the size) and optical properties
200 (including the SSA and the ASY) are simulated by the SBDART model. The impacts of the
201 microphysical properties and the optical properties of the dust aerosol on the $DRFE_{dust}$ at the TOA are
202 analyzed in this study.

203 **2.2 Data**

204 This paper aims to analyze the differences in dust microphysical properties and the $DRFE_{dust}$ at the
205 TOA over the Taklimakan Desert and the Sahara Desert to confirm the influences of dust aerosol
206 microphysical properties on simulating the $DRFE_{dust}$. Also, the advantages of the satellite-based
207 method in estimating the $DRFE_{dust}$ at the TOA are analyzed. Therefore, the $DRFE_{dust}$ over the
208 Taklimakan Desert and the Sahara Desert is estimated by using both satellite observations and dust
209 microphysical properties.



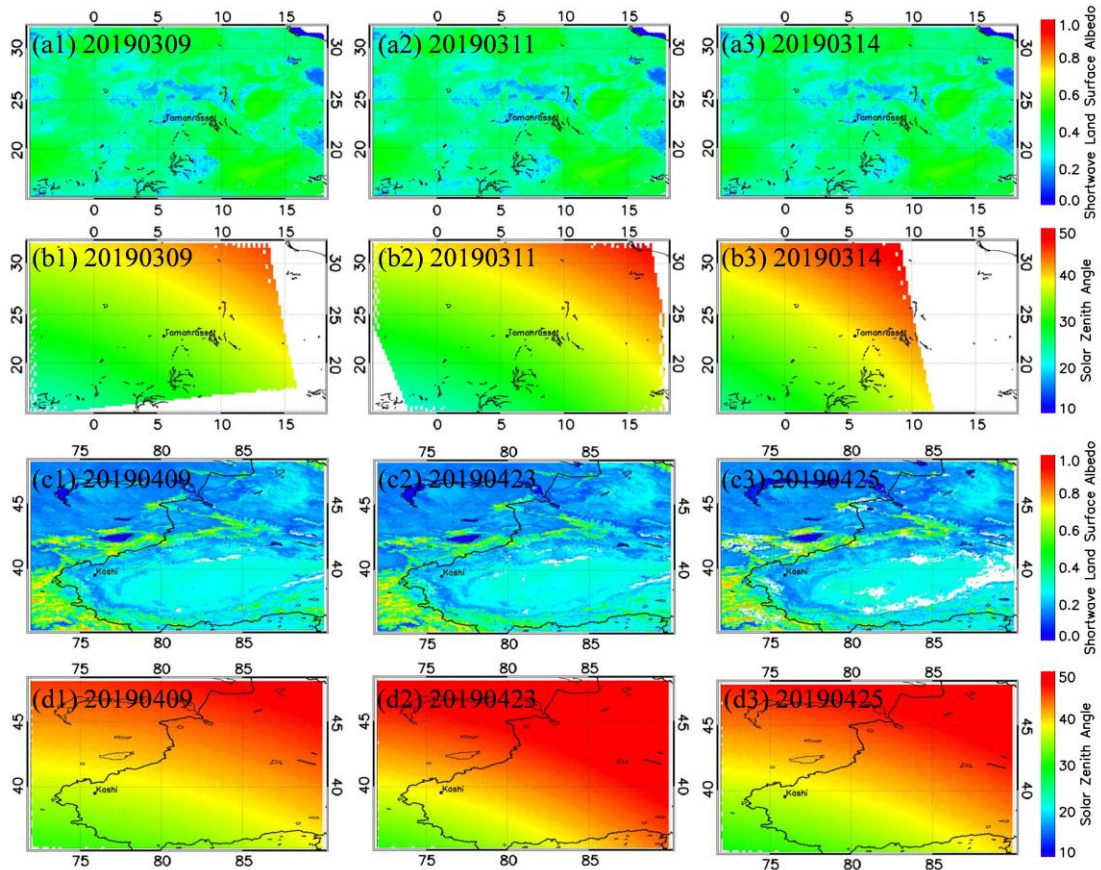
210

211 **Figure 2: The research regions and dust storms viewed by MODIS AQUA on 11 March and 9 April 2019.**

212 Fig. 2 shows the research regions (the red square areas) and the locations of in-situ sites
 213 (Tamanrasset site and Kashi site, the red dots in the map and satellite images). Tamanrasset (22.79°N,
 214 5.53°E, 1377 m above the mean sea level) locates in southern Algeria, which is free from the influence
 215 of industrial activities. Thus, the aerosols measured in Tamanrasset can represent the pure dust aerosols
 216 from the Sahara Desert around Tamanrasset (Guirado-Fuentes et al., 2014). Kashi (39.5°N, 75.9°E,
 217 1320 m above the mean sea level) locates in the vicinity of the Taklimakan Desert. Kashi represents a
 218 place affected by dust aerosols transported from the Taklimakan Desert (Li et al., 2020). Thus, dust
 219 aerosols observed in Tamanrasset and Kashi sites are typical samples of the dust aerosols around these
 220 two sites in the Sahara Desert and Taklimakan Desert. Moreover, Tamanrasset and Kashi sites are
 221 similar in land surface type, altitude, and climate. As the LSA and the SZA have a great impact on the
 222 SW radiative effect, the regions with similar LSA and SZA are chosen to avoid the influence of different
 223 LSA and SZA on evaluating the differences of dust microphysical properties and dust radiative effect
 224 from different dust source regions.

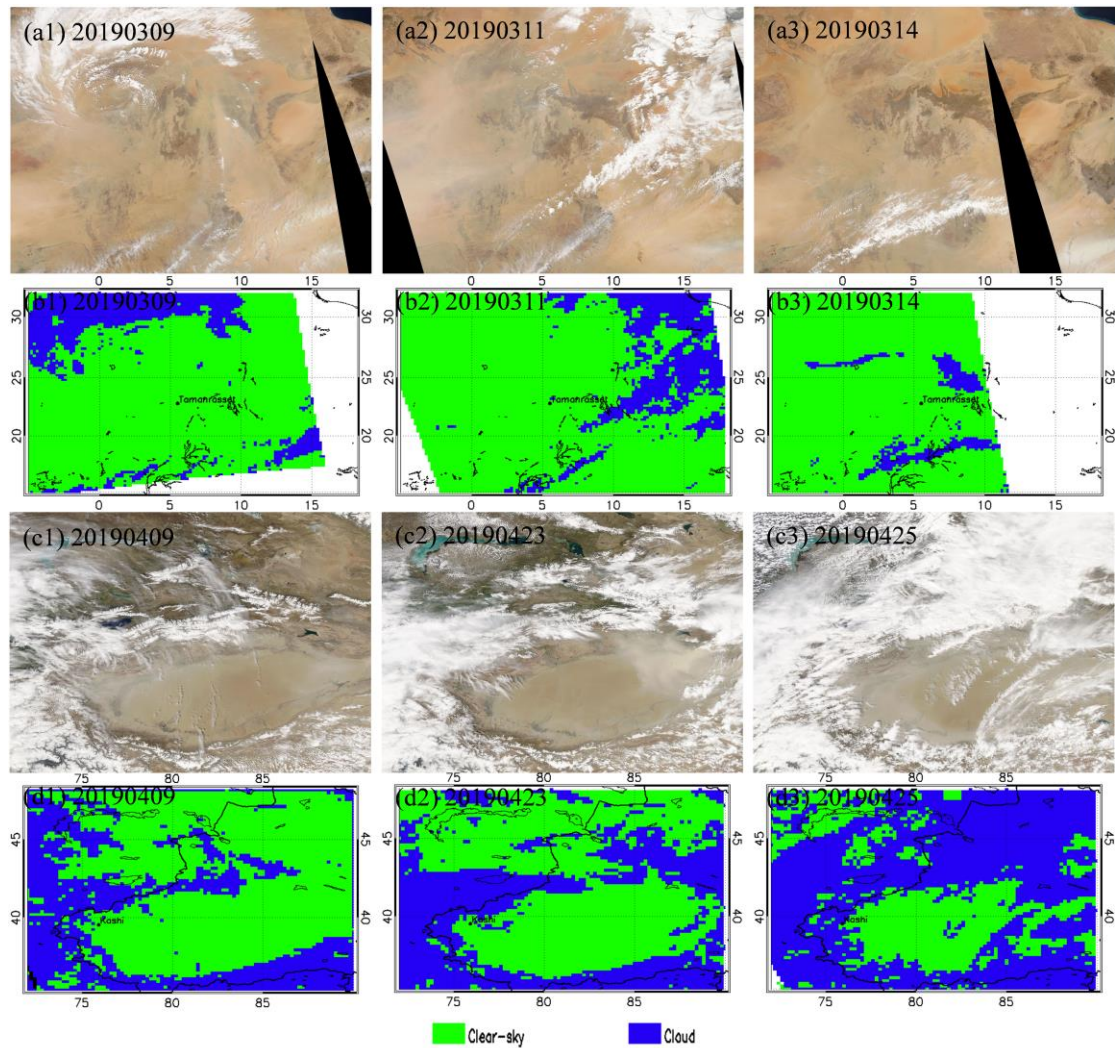
225 Several dust storms occurred on March 9, 11 and 14, 2019 in the Sahara Desert. In the Taklimakan
 226 Desert, dust storms occurred on April 9, 23 and 25, 2019. Figure 3 shows the LSA and the SZA
 227 observed by the AQUA satellite over the Sahara Desert (Figs. 3(a1)–(a3) and Figs. 3(b1)–(b3)) and
 228 Taklimakan Desert (Figs. 3(c1)–(c3) and Figs. 3(d1)–(d3)) during dust storm episodes. In Fig. 3, the
 229 LSA and the SZA are similar in Tamanrasset and Kashi when the satellite passes through. The data

230 around Tamanrasset and Kashi in March and April are suitable for analyzing the differences of dust
 231 microphysical properties and their influences on the $DRFE_{dust}$.



232
 233 **Figure 3: SW LSA and SZA over the Sahara Desert and the Taklimakan Desert derived from**
 234 **AQUA/MODIS.**

235 Figs. 4(a1)–(a3) and Figs. 4(c1)–(c3) present the true color images over the Sahara Desert and the
 236 Taklimakan Desert, respectively. Figs. 4(b1)–(b3) and Figs. 4(d1)–(d3) respectively present the cloud
 237 detections over the Sahara Desert and the Taklimakan Desert from AQUA/MODIS observations. The
 238 satellite crossed over the Sahara Desert on March 9 (UTC 13:05), 11(UTC 12:55) and 14 (UTC 13:20),
 239 2019, and crossed over the Taklimakan Desert on April 9 (07:30), 23 (07:40) and 25 (07:30), 2019. The
 240 true color images and cloud detections clearly show that, the Tamanrasset site and Kashi site were not
 241 covered by clouds during these dust storms. The satellite-observed and dust microphysical property data
 242 of the dust storms in March and April 2019 in Tamanrasset and Kashi are collected to analyze the dust
 243 microphysical properties and estimate the $DRFE_{dust}$ in the Sahara Desert and the Taklimakan Desert.
 244 Both the satellite data and synergy dust microphysical properties data are collected around Tamanrasset
 245 and Kashi sites for analyzing the differences in dust microphysical properties and estimating the



247

248 **Figure 4: True color images and cloud detections from AQUA/MODIS observations.**249 **2.2.1 Satellite data**

250 MODIS and CERES are the key instruments of the AQUA and the TERRA satellite and are
 251 important in NASA's Earth Observing System (EOS). The AOD products from MODIS and the
 252 radiative flux products at the TOA from CERES can be synergistically used to estimate the DRFE_{dust}
 253 directly.

254 Several algorithms have been developed for MODIS AOD remote-sensing products after MODIS
 255 instruments were launched (Remer et al., 2005). Of these algorithms, the Deep Blue algorithm (Hsu et
 256 al., 2004) solved the problems in aerosol retrieval by satellite remote-sensing for high reflectance land
 257 surface types (such as arid, semi-arid, and desert areas), and retrieved the AOD over high reflectance
 258 land surface types. In this paper, the deep blue AOD (0.55 μ m) data are used to discriminate the dust

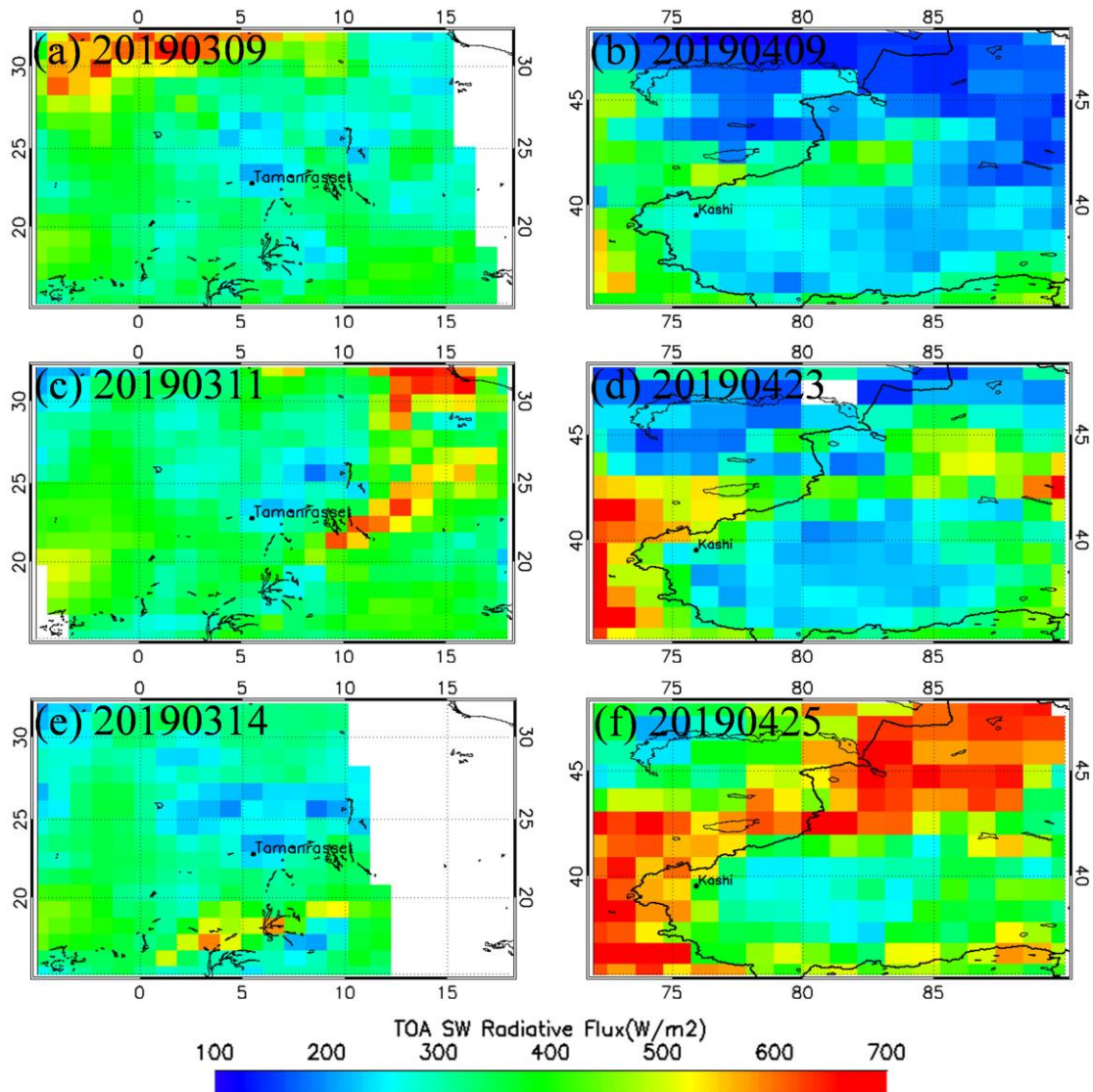
259 storm regions. Since the Sahara Desert and the Taklimakan Desert are free of industrial activities, the
260 major aerosol over the desert areas is dust aerosol, and the anthropogenic and marine aerosols have
261 little contribution to the total AOD, especially during dust storm episodes. Thus, we directly use the
262 AOD retrieved by MODIS to estimate $DRFE_{\text{dust}}$ during dust storms in this study. The LSA is also
263 needed both in the satellite-based equi-albedo method and the RTM. The MODIS Collection6 albedo
264 product dataset (MCD43C3) (Schaaf et al., 2011;Schaaf et al., 2002a;Schaaf et al., 2008) provides
265 high-quality land surface reflectance and albedo data over various types of land surfaces by using
266 anisotropy retrievals algorithm (Jin et al., 2003;Liang et al., 2002;Liu et al., 2009;Román et al., 2010).
267 The MCD43C3 product dataset is available from the Land Processes Distributed Active Archive Center
268 (LP DAAC) of NASA. The SW white-sky albedo (WSA) and black-sky albedo (BSA) from the
269 MCD43C3 product are used to get the SW broadband (0.3–5.0 μm) LSA. BSA and WSA mark the
270 extreme cases of completely direct and completely diffuse illumination. Here, the LSA is calculated by
271 interpolating from BSA and WSA (Lewis and Barnsley, 1994;Schaaf et al., 2002b).

272 The CERES Single Scanner Footprint (SSF) Level 2 instantaneous SW Flux data is available at
273 <http://ceres.larc.nasa.gov>. The CERES SSF is a unique product for studying the role of clouds, aerosols
274 and radiation in climate. CERES single scanner footprint (SSF) level 2 dataset can provide the radiative
275 flux at the TOA in three broadband channels. The radiative flux derived from CERES is co-located
276 with the MODIS scene. Here the instantaneous SW channel (0.3–5.0 μm) radiative flux at the TOA
277 from CERES SSF level 2 dataset is used. MODIS and CERES are onboard in the same satellite
278 platform (AQUA). The DRE_{dust} and the $DRFE_{\text{dust}}$ at the TOA are estimated by synergistically using
279 MODIS and CERES products.

280 **2.2.2 Dust microphysical property data**

281 The Aerosol Robotic Network (AERONET) (Holben et al., 1998) is the largest ground-based
282 network for measuring aerosols with more than 400 sites installed.

283 The AERONET provides microphysical properties and optical properties of the aerosols at four
284 wavelengths (440, 675, 870, and 1020 nm). The AOD product is directly measured by the sun
285 photometer. The inversion algorithm retrieves the physical properties of aerosols such as volume size
286 distributions and the complex refractive index, and optical properties such as the SSA and the ASY
287 (Dubovik and King, 2000;Dubovik et al., 2006).

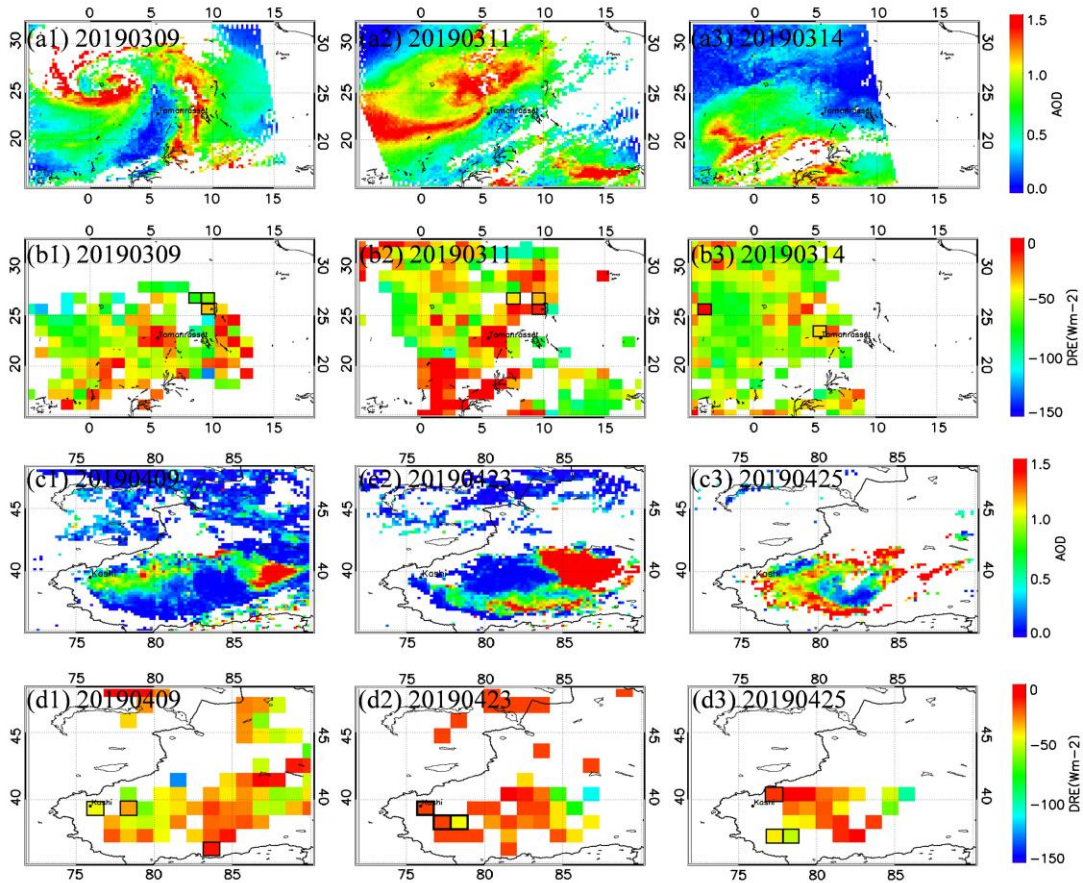


289
 290 **Figure 5: TOA SW radiative flux derived from AQUA/CERES over the Sahara Desert on March 2019 and**
 291 **over the Taklimakan Desert on April 2019.**

292 Figure 5 shows the TOA SW radiative flux measured by CERES over the Sahara Desert in March
 293 2019 and that over the Taklimakan Desert in April 2019 during the dust storm episodes. The TOA SW
 294 radiative flux distribution shows the highest value over cloud conditions (the cloud regions can be
 295 found from Fig. 4). The values in dust storm regions are higher than those in clear-sky regions. It is due
 296 to the SW albedo of the dust aerosols and cloud is higher than the land surface albedo.

297 As shown in Fig. 3, Fig. 5 and Fig. 6, the spatial resolution of TOA flux from CERES/SSF
 298 product is 1°×1°, and LSA, SZA, AOD data from satellite have the different spatial resolutions. In order
 299 to match up LSA, SZA and AOD data with CERES TOA SW fluxes, we have resampled LSA, SZA
 300 and AOD data following the horizontal spatial resolution of CERES SSF products. Following the

301 equi-albedo method (Tian et al., 2019), the F_{clr} and DRE_{dust} over the Sahara Desert and the
 302 Taklimakan Desert can be estimated based on the measurements from MODIS and CERES both aboard
 303 on the AQUA satellite.



304
 305 **Figure 6: AOD and DRE_{dust} of dust storms over the Sahara Desert in March 2019 and over the**
 306 **Taklimakan Desert in April 2019.**

307 MODIS L2 deep blue AOD products of the dust storm over the Sahara Desert in March 2019 and
 308 that over the Taklimakan Desert in April 2019 are shown in Fig. 6(a1)–(a3) and Figs. 6(c1)–(c3),
 309 respectively. The missing data are shown in white; the high dust loading regions are shown in red; the
 310 low dust loading regions are shown in blue. The AOD distribution maps show that there were heavy
 311 dust storms over the Sahara Desert and the Taklimakan Desert with AOD great than 1.0 detected by
 312 MODIS.

313 Figs. 6(b1)–(b3) and Figs. 6(d1)–(d3) show the distribution maps of the DRE_{dust} at the TOA. The
 314 high dust aerosol loading regions show significant negative radiative forcing. It indicates that the dust
 315 aerosol loading is negatively correlated with the DRE_{dust} in these dust storm events. Thus, dust aerosols
 316 have a negative radiative effect in the SW spectrum. The distribution maps of the LSA and the SZA

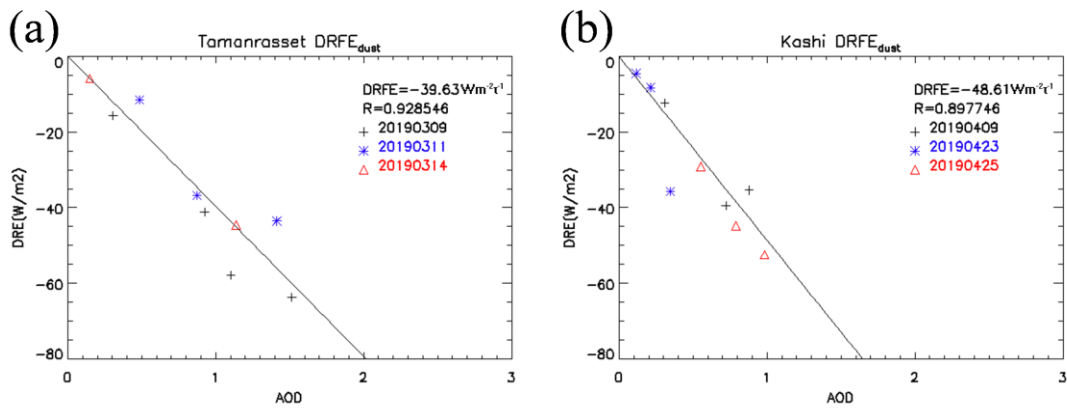
317 (Fig. 3) show that the mean SW LSA measured by MODIS is around 0.18 and the mean SZA is around
318 35 degrees in Tamanrasset and Kashi. The distribution maps also show that the LSA and SZA vary
319 greatly in the same satellite scan image. In our previous study, we found that DRE_{dust} at the TOA was
320 significantly influenced by LSA and SZA (Tian et al., 2019). To avoid the influence of the LSA and
321 SZA in estimating the $DRFE_{dust}$, we estimate $DRFE_{dust}$ using pixels with similar LSAs and SZAs.
322 Furthermore, the values of AOD and cloud could also influence the regions we selected. The deep blue
323 algorithm retrieved AOD has large uncertainties in the small value areas. The cloud-free pixels with
324 AOD great than 0.1, and with the LSA of 0.16–0.20 and the SZA of 32–38 degrees are chosen to
325 estimate the $DRFE_{dust}$. Therefore, only few pixels having similar values of the LSA and the SZA at
326 Tamanrasset and Kashi are picked for estimating the DRE_{dust} and $DRFE_{dust}$ at the TOA. These chosen
327 pixels are surrounded by black border in Figs. 6(b1)–(b3) and Figs. 6(d1)–(d3). The influences of the
328 dust microphysical properties on the $DRFE_{dust}$ are investigated. These pixels of the DRE_{dust} and its
329 co-located AOD values are illustrated in Table 1.

330 **Table 1: DRE_{dust} at the TOA and AOD over the Sahara Desert in March 2019 and that over the**
331 **Taklimakan Desert in April 2019 during the dust storms.**

Regions & Dates		Properties	AOD	DRE_{dust}	
Sahara Desert	20190309		0.92	-41.2	
			1.51	-63.7	
			1.11	-57.8	
			0.31	-15.6	
			0.48	-11.5	
	20190311		1.41	-43.5	
			0.87	-36.7	
		20190314		1.14	-44.6
				0.15	-5.8
		Taklimakan Desert	20190409		0.31
			0.72	-39.5	
			0.88	-35.4	
20190423			0.21	-8.3	

	0.35	-35.7
	0.11	-4.5
20190425	0.79	-44.8
	0.98	-52.4
	0.55	-29.1

332 According to the definition, the $DRFE_{dust}$ represents the DRE_{dust} of per unit AOD during these
333 storms in the dust source regions. Therefore, the $DRFE_{dust}$ can be estimated by fitting the DRE_{dust} and
334 the AOD.

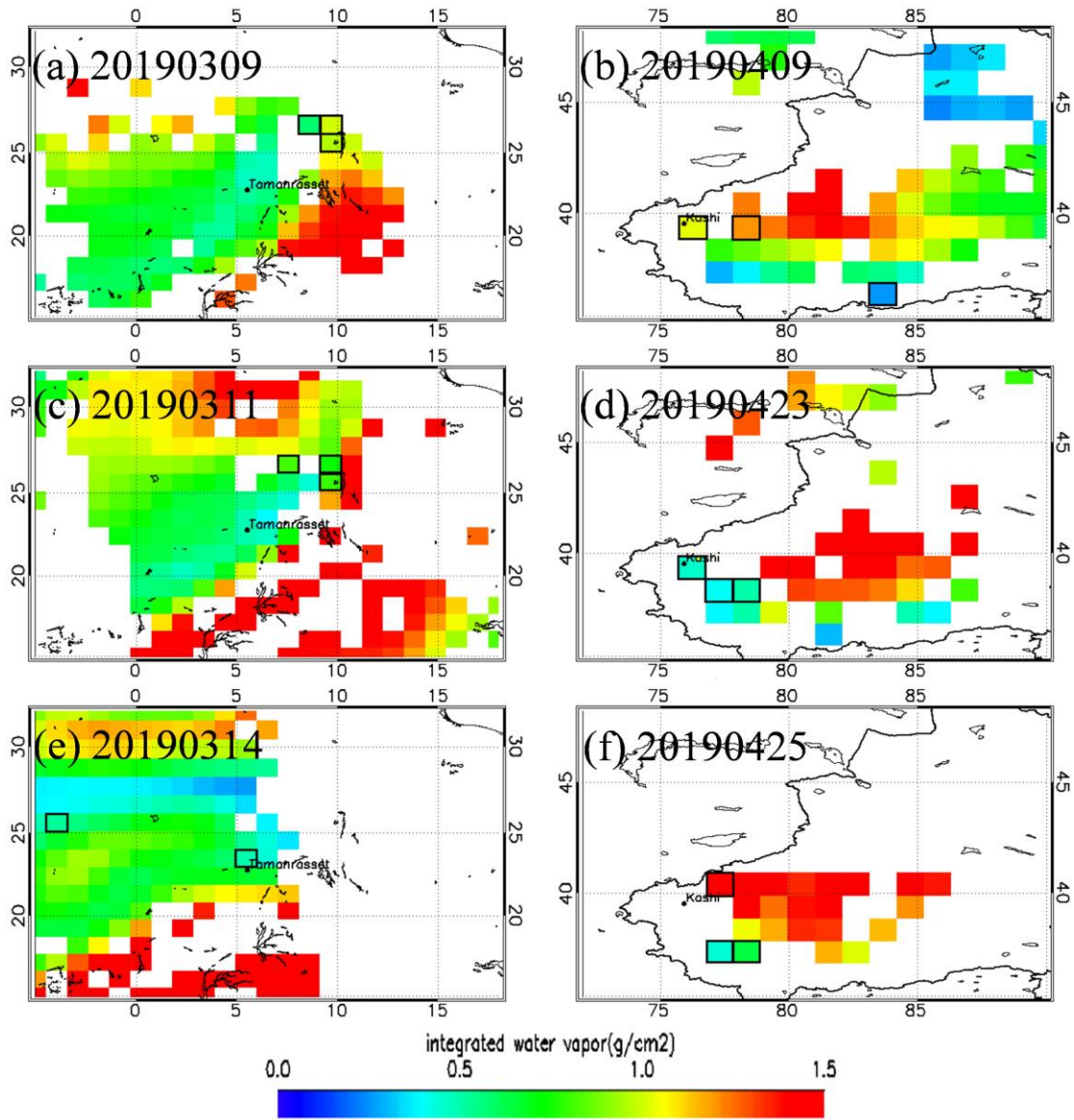


335
336 **Figure 7: DRE_{dust} in (a) March 2019 over Tamanrasset and (b) April 2019 over Kashi.**

337 The linear relationship between the DRE_{dust} and the AOD ($0.55\mu m$) can be found during dust
338 storms around Tamanrasset and Kashi, which is also investigated in previous studies (Kumar et al. 2015;
339 Jose et al. 2016). Then, the $DRFE_{dust}$ can be estimated by regressing the DRE_{dust} and the AOD. In Fig. 7,
340 the mean $DRFE_{dust}$ of the dust storms is $-39.6 Wm^{-2}\tau^{-1}$ over Tamanrasset and $-48.6 Wm^{-2}\tau^{-1}$ over
341 Kashi. The correlation coefficients are high with $R = 0.92$ in March 2019 over Tamanrasset and $R =$
342 0.89 in April 2019 over Kashi. The AOD and DRE_{dust} values are well correlated. Positive dust AOD is
343 associated with negative DRE_{dust} .

344 The equi-albedo method directly estimates the DRE_{dust} and the $DRFE_{dust}$ based on the satellite
345 observations. Therefore, the accuracy of the results (DRE_{dust} and $DRFE_{dust}$) derived from the
346 equi-albedo method is highly dependent on the accuracy of satellite observations. Therefore, the
347 uncertainties of the $DRFE_{dust}$ derived from the equi-albedo method mainly include the instantaneous
348 SW flux error from CERES measurements, the estimation uncertainties of the F_{clr} over the dust storm
349 region, and the uncertainty in the deep blue AOD product. Besides, according to our sensitivity test in

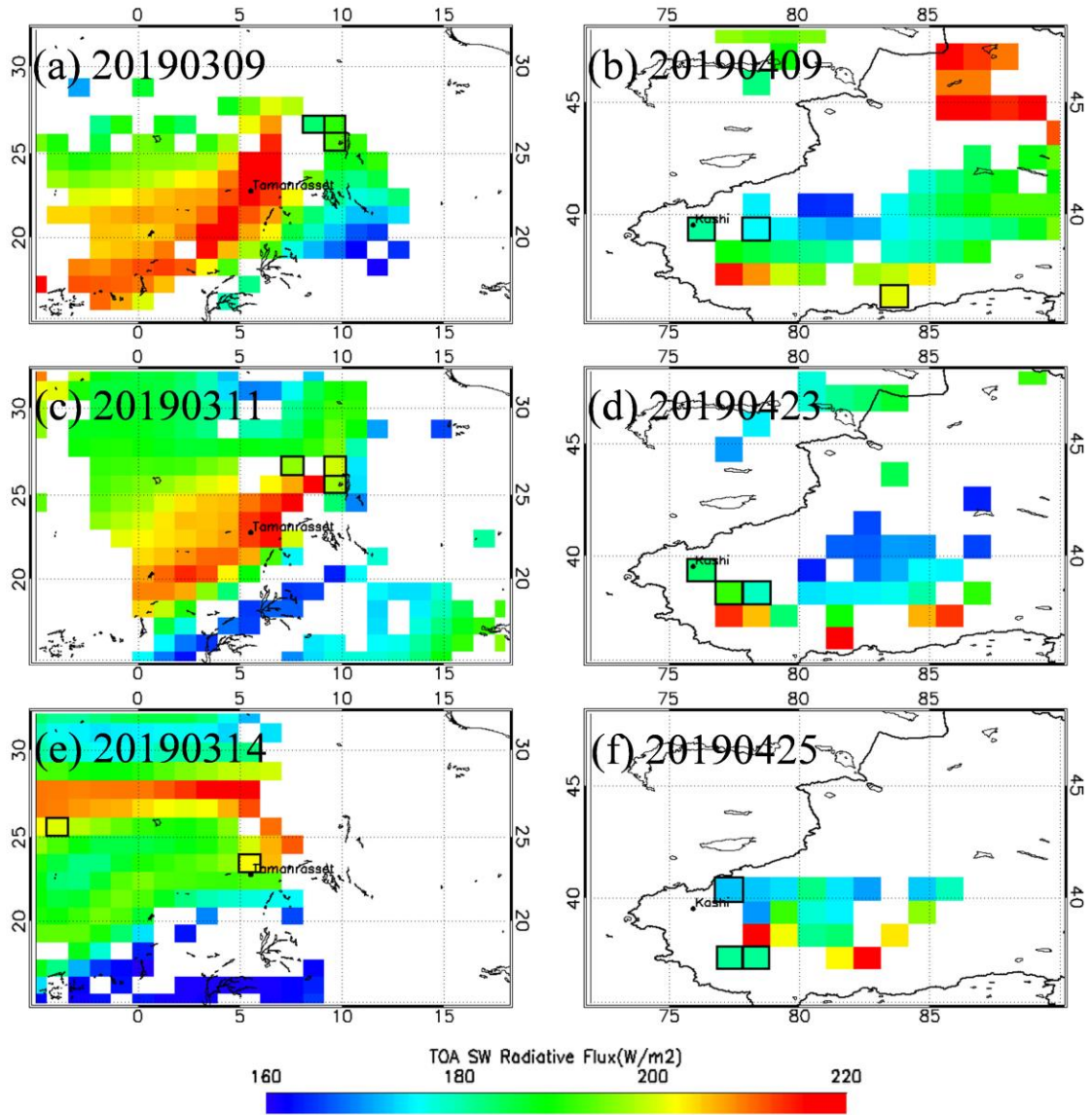
350 the previous study (Tian et al., 2019), the atmospheric profile, water vapor and height of dust layer
 351 have insignificant influence on SW radiative flux at the TOA. It is reasonable to use same water vapor
 352 and pre-defined vertical distribution for dust aerosols in one scene of satellite data. However, the
 353 assumption of pixels has same water vapor and pre-defined aerosol vertical distribution over one scene
 354 of satellite data still cause small uncertainties.



355
 356 **Figure 8: Integrated water vapor (g/cm^2) from European Centre for Medium-range Weather**
 357 **Forecasts (ECMWF) reanalysis dataset over the Sahara Desert in March 2019 and over the Taklimakan**
 358 **Desert in April 2019.**

359 Fig.8 shows the integrated water vapor from ECMWF reanalysis dataset over the Sahara Desert in
 360 March 2019 and over the Taklimakan Desert on April 2019. The grids surrounded by black border are
 361 the chosen pixels to estimate the $\text{DRFE}_{\text{dust}}$. The integrated water vapor varies little over different

362 research areas, and the mean differences of chosen pixels are 0.51g/cm^2 and 0.18g/cm^2 over the Sahara
 363 Desert and the Taklimakan Desert, respectively. In order to estimate the uncertainties caused by the
 364 variation of integrated water vapor over chosen pixels, we have calculated the SW radiative flux at the
 365 TOA under different integrated water vapor based on the SBDART model.

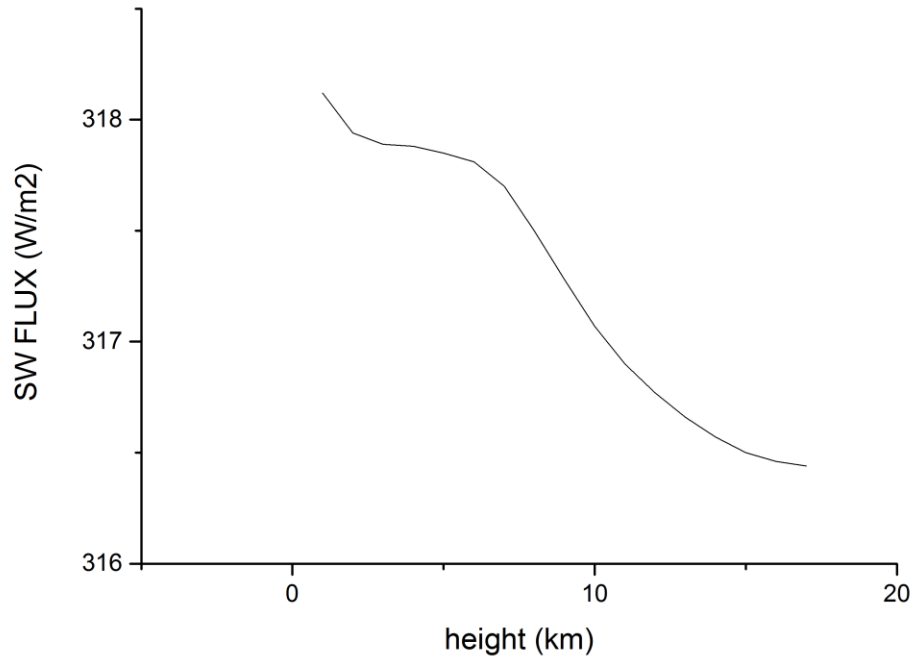


366
 367 **Figure 9: SBDART simulated clear-sky TOA radiative flux by using integrated water vapor (g/cm^2) from**
 368 **ECMWF reanalysis dataset over the Sahara Desert in March 2019 and over the Taklimakan**
 369 **Desert in April 2019.**

370 Fig. 9 shows the SBDART simulated clear-sky TOA radiative flux by using the integrated water
 371 vapor from ECMWF reanalysis dataset over the Sahara Desert in March 2019 and over the Taklimakan
 372 Desert in April 2019, and the grids surrounded by black border are the chosen pixels to derive the
 373 $\text{DRFE}_{\text{dust}}$. The regional mean differences of TOA radiative flux are 2.21% and 0.85% over the Sahara

374 Desert and the Taklimakan Desert, respectively. This indicates the variation of integrated water vapor
 375 cloud cause uncertainties of TOA radiative flux by 2.21% and 0.85% over the Sahara Desert and the
 376 Taklimakan Desert.

377 For the assumption of vertical profile for dust aerosols, we have also tested the sensitivity of
 378 radiative flux at the TOA to various heights of dust layer with the SBDART model.



379
 380 **Figure 10: The sensitivity test of SW radiative flux at the TOA to various heights of dust layer.**

381 As shown in Fig. 10, the SW radiative flux at the TOA decreases with the increase of the height of
 382 dust layer. However, the SW radiative flux changes little (within 1.5Wm^{-2} , 0.47%) with the increase of
 383 the height of dust layer.

384 According to our previous study (Tian et al., 2019), the instantaneous SW flux error from CERES
 385 measurements is about 3.13%, the estimation uncertainty of the F_{clr} is 3.15%, the uncertainty of the
 386 deep blue AOD retrieved by MODIS is about 15% (Sayer et al., 2014). Over one scene of satellite data,
 387 the uncertainties of using same water vapor in Kashi and Tamanrasset are 2.21% and 0.85%,
 388 respectively, and the uncertainty caused by pre-defined aerosol vertical distribution is also estimated,
 389 which is about 0.47%. Then, the total uncertainties of the $\text{DRFE}_{\text{dust}}$ can be calculated by the equation
 390 Eq. (3) (Zhang et al., 2005).

391
$$U_t = \exp[\sum(\log U_s)^2]^{1/2} \tag{3}.$$

392 U_s is the synthetical uncertainty factor of each source of the uncertainty (including the
393 instantaneous SW flux error from CERES measurements, the estimation uncertainty of the F_{clr} , and the
394 uncertainty of the deep blue AOD retrieved by MODIS). U_t is the total uncertainty of the $DRFE_{dust}$,
395 which is 25.37% and 28.19% ($10.0 \text{ Wm}^{-2}\tau^{-1}$ and $13.7 \text{ Wm}^{-2}\tau^{-1}$) in Tamanrasset and Kashi, respectively.
396 Therefore, the $DRFE_{dust}$ are $-39.6 \pm 10.0 \text{ Wm}^{-2}\tau^{-1}$ in March 2019 over Tamanrasset and -48.6 ± 13.7
397 $\text{Wm}^{-2}\tau^{-1}$ in April 2019 over Kashi.

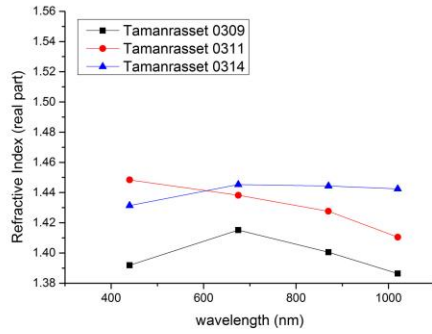
398 **4 Deriving $DRFE_{dust}$ from the RTM simulations**

399 **4.1 Dust microphysical properties**

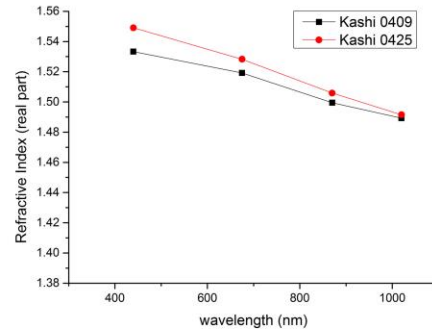
400 The inversion of sun-photometry optical data to obtain particle microphysical properties has been
401 done through numerous approaches. Currently, the AERONET inversion algorithm makes use of direct
402 sun and sky radiance measurements (Dubovik et al., 2006; Dubovik and King, 2000).

403 The focuses of this paper are the differences in the dust microphysical properties from different
404 dust source regions and the impacts of the dust microphysical properties on the $DRFE_{dust}$ simulation. As
405 important parameters concerning the radiative impacts, the volume size distribution and the refractive
406 index of the dust aerosol are compared in the dust storms over Tamanrasset and Kashi.

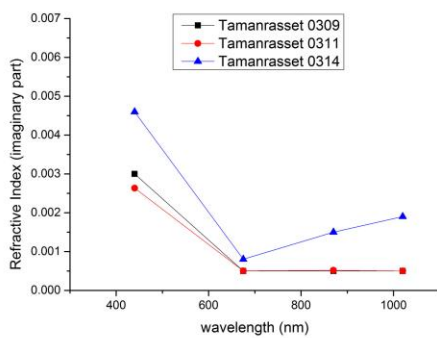
(a) Real parts of the complex refractive index over Tamanrasset in the Sahara Desert



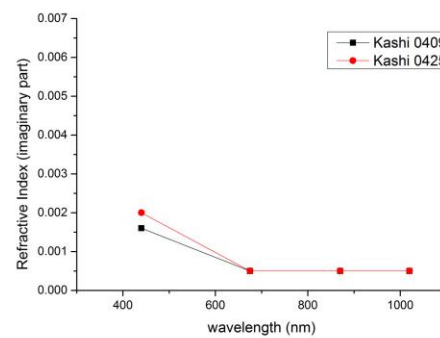
(b) Real parts of the complex refractive index over Kashi in the Taklimakan Desert



(c) Imaginary parts of the complex refractive index over Tamanrasset in the Sahara Desert



(d) Imaginary parts of the complex refractive index over Kashi in the Taklimakan Desert



407

408

Figure 11: Real and imaginary parts of the dust complex refractive index over Tamanrasset in the Sahara Desert and Kashi in the Taklimakan Desert.

409

410

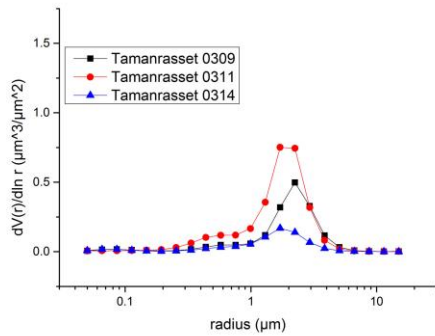
The refractive index is a measurement of the aerosol refraction and absorption efficiency. Aerosols with high real parts of the complex refractive index values are indicated to be scattering types. Conversely, aerosols with high imaginary parts are indicated to be absorbing types (Zhang et al., 2006). Figure 11 shows the real and imaginary parts of the dust complex refractive index over Tamanrasset in the Sahara Desert and Kashi the Taklimakan Desert during the dust storms. In Fig. 11, dust aerosols over Kashi have higher real parts (Fig. 11 (b)) and lower imaginary parts (Fig. 11 (d)) than aerosols over Tamanrasset (Fig. 11 (a) and Fig. 11 (c)), showing that the dust aerosols over Kashi in the Taklimakan Desert have stronger scattering effects.

418

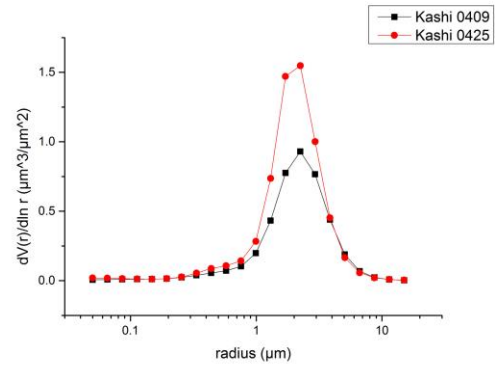
Figure 12 illustrates the variation of the dust aerosol size distribution during the dust storms over Tamanrasset in March 2019 and over Kashi in April 2019. Most maximum dust aerosol size distribution peaks at the radius of $1.71\mu\text{m}$ in Tamanrasset and $2.24\mu\text{m}$ in Kashi. Moreover, the peak values are higher in Kashi. It is indicated that the dust storm was stronger in Kashi in April 2019, and the coarse mode aerosol particles increased in particle volume compared with those in the dust storm in Tamanrasset in March 2019.

423

(a) Dust aerosol size distribution over Tamanrasset in the Sahara Desert



(b) Dust aerosol size distribution over Kashi in the Taklimakan Desert



424

425 **Figure 12: Dust aerosol size distribution over (a) Tamanrasset in the Sahara Desert and (b) Kashi in the**
426 **Taklimakan Desert.**

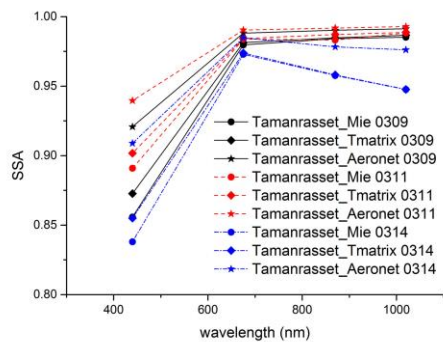
427 4.2 Dust optical properties

428 The dust optical properties can be calculated by synergistically using the real and imaginary parts of
429 the dust complex refractive index and the dust aerosol size distribution.

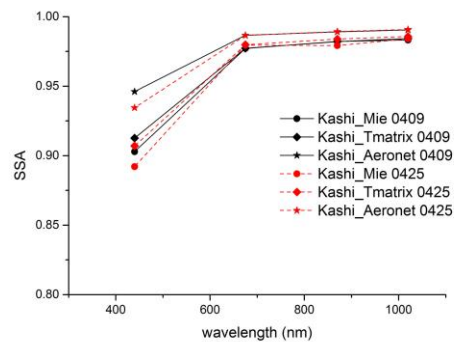
430 The SSA and the ASY are two key parameters determining the DRE_{dust} and the $DRFE_{dust}$. Accurate
431 measurements of the SSA and the ASY are important for the assessment of the direct effect of aerosols
432 on climate (Qie et al., 2019). The dust aerosol optical properties are calculated by using the Mie theory,
433 the T-matrix method, and the AERONET inversion products (Dubovik and King, 2000; Dubovik et al.,
434 2006).

435 The SSA is presented as the ratio between the aerosol scattering and extinction coefficients. The
436 dust SSA describes the scattering properties of the dust aerosols. The SSA can largely determine the
437 magnitudes and signs of the DRE_{dust} and the $DRFE_{dust}$. Strongly scattering dust aerosols (i.e., $SSA = 1$)
438 always cause negative DRE_{dust} . By contrast, low SSA aerosols often cause positive DRE_{dust} , especially
439 over high LSA regions as the light absorbed by the aerosols can reduce the cooling effect. The size
440 distribution and the complex refractive index can codetermine the magnitude of the SSA.

(a) Single Scattering Albedo of dust aerosols over Tamanrasset in the Sahara Desert



(b) Single Scattering Albedo of dust aerosols over Kashi in the Taklimakan Desert

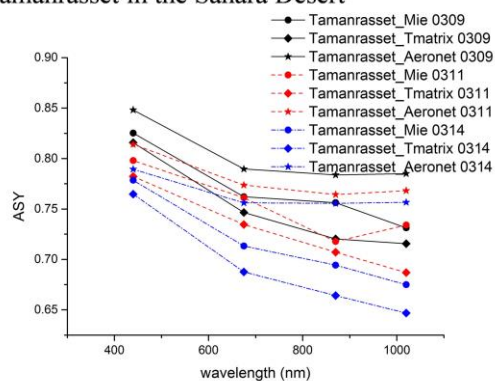


441

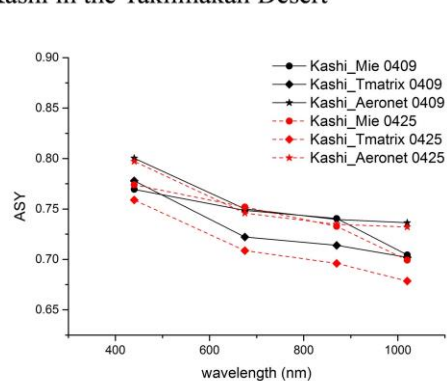
442 **Figure 13: Single scattering albedo of dust aerosols over (a) Tamanrasset in the Sahara Desert and (b) Kashi**
 443 **in the Taklimakan Desert.**

444 Figure 13 shows the variabilities of the dust aerosol SSA between different dust source regions and
 445 different calculation methods. In Fig. 13, the maximum SSA value mostly occurs at the wavelength of
 446 1020 nm, which indicates that the SSA is dependent on wavelength. Moreover, dust aerosols from the
 447 Taklimakan Desert (Kashi) in the figure have higher SSA value using both the Mie theory and the
 448 T-matrix method. The higher value of SSA shows that dust aerosol particles scatter more
 449 predominantly and strongly in the Taklimakan Desert (Kashi), which may cause more significant
 450 negative radiative effect than the dust aerosols over Tamanrasset.

(a) Asymmetry factor of dust aerosols over Tamanrasset in the Sahara Desert



(b) Asymmetry factor of dust aerosols over Kashi in the Taklimakan Desert



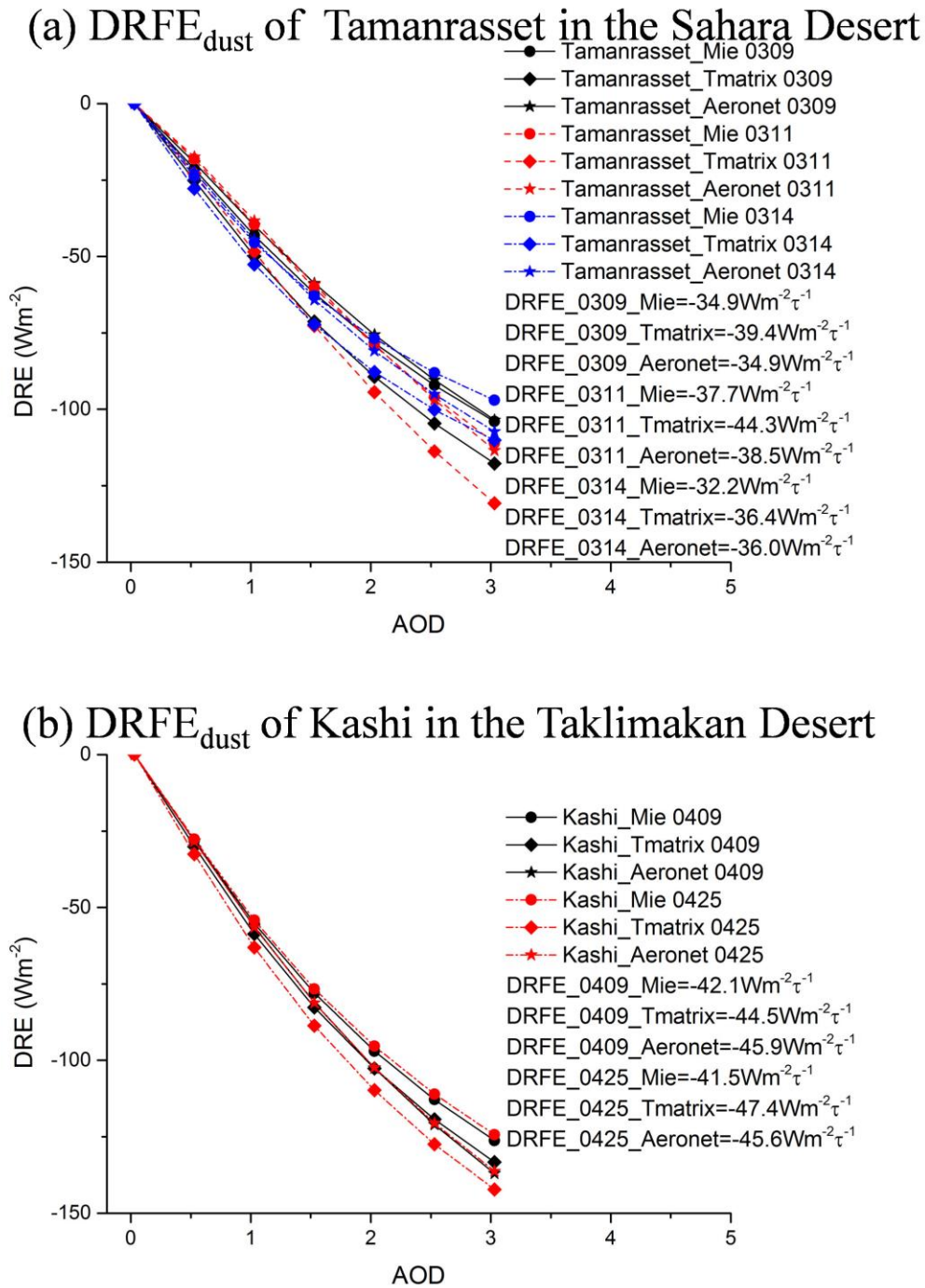
451

452 **Figure 14: Asymmetry factor of dust aerosols over (a) Tamanrasset in the Sahara Desert and (b) Kashi in**
 453 **the Taklimakan Desert.**

454 The ASY indicates the relative strength of the forward scattering, which determines the integrated
 455 fractions of the energy that scatter backward and forward. The dust aerosol particles with sharp peaks in
 456 the forward direction (0° scattering angle) have positive ASY. The ASY value increases with the
 457 particle size.

458 The ASY in Fig. 14 shows marked spectral variation with higher values at shorter wavelengths. It
459 can be found that the dust aerosols from the Sahara Desert (Tamanrasset) have higher values of the ASY
460 than those from the Taklimakan Desert (Kashi) in both the Mie theory and the T-matrix method. The
461 stronger backward scattered energy may cause higher negative radiative effect over Kashi.

462 According to the analyses of the microphysical properties and the optical properties, the dust
463 aerosols over Kashi scatter strongly. The negative $DRFE_{\text{dust}}$ of Kashi should be more significant than
464 those of Tamanrasset. The results are in good agreement with those estimated by the satellite
465 observations.



467

468 **Figure 15: DRFE_{dust} simulated by the SBDART over (a) Tamanrasset in the Sahara Desert and (b) Kashi in**
 469 **the Taklimakan Desert.**

470 The DRFE_{dust} estimated directly by the satellite observation is compared with that simulated by the
 471 SBDART to verify the reliability. As shown in Fig. 15, with higher aerosol scattering (higher SSA in
 472 Fig. 13) and higher backward scattering (lower ASY in Fig. 14), the negative DRFE_{dust} from Kashi is

473 more significant. The mean $DRFE_{dust}$ from Tamanrasset is $-37.1 \text{ W m}^{-2} \tau^{-1}$. The dust aerosols from
 474 Kashi have stronger cooling effects than those from Tamanrasset, in which the mean $DRFE_{dust}$ is -44.5
 475 $\text{W m}^{-2} \tau^{-1}$. The results are in good agreement with those estimated by the satellite observations. The
 476 $DRFE_{dust}$ estimated by the dust optical properties derived from the T-matrix method and the
 477 AERONET is closer to those estimated by the satellite observations, which indicates that most dust
 478 aerosols are non-spherical in the natural environment.

479 The results also show that the dust microphysical properties can significantly influence the
 480 $DRFE_{dust}$. The mean difference of the $DRFE_{dust}$ between Tamanrasset and Kashi (difference between
 481 the mean $DRFE_{dust}$ in Tamanrasset and in Kashi) is 18.14% ($7.4 \text{ W m}^{-2} \tau^{-1}$). Even for the same size
 482 distributions and the complex refractive index of dust aerosol, the $DRFE_{dust}$ varies significantly
 483 according to whether the dust particles are considered spherical or non-spherical in different methods.
 484 For the differences of the $DRFE_{dust}$ estimated using different methods, the mean standard deviations are
 485 7.6% ($2.8 \text{ W m}^{-2} \tau^{-1}$) in Tamanrasset and 6.8% ($3.0 \text{ W m}^{-2} \tau^{-1}$) in Kashi. Moreover, Li et al. (2020)
 486 pointed out that the atmospheric profile, LSA and SZA, can also influence the simulation of the
 487 instantaneous $DRFE_{dust}$, which agrees with our previous study (Tian et al., 2019). Additionally, it is
 488 difficult for climate models or in-situ measurements to get the real distribution of the aerosol properties
 489 at a large spatial extent. Also, it is hard to evaluate the uncertainties in radiative transfer simulations. It
 490 can cause significant errors in evaluating the modulating effects of the mineral dust aerosols on climate
 491 (Huang et al., 2009; Li et al., 2020).

492 **5 $DRFE_{dust}$ in the satellite-based observation and the simulation of the RTM**

493 According to the analyses of the dust aerosol microphysical properties and optical properties, the
 494 dust aerosols from the Taklimakan Desert (Kashi) should scatter strongly. The RTM simulation results
 495 are in good agreement with the results estimated by the satellite observation. Previous studies also
 496 estimated the $DRFE_{dust}$ in the Sahara Desert and the Taklimakan Desert (Li et al., 2020; Li et al.,
 497 2004; Garc ía et al., 2012; Xia and Zong, 2009), which validate our results.

498 **Table 2: SW $DRFE_{dust}$ from different studies.**

Dust source regions	Research	Model/Method	$DRFE_{dust}$ ($\text{Wm}^{-2}\tau^{-1}$)	Description
Sahara	Li et al (2004)	Satellite+SBD	-35 ± 3 (summer)	Binned mean

Desert	Method	Value	Notes
	ART	-26 ± 3 (winter)	fitting TOA diurnal mean $DRFE_{dust}$ over the Atlantic Ocean near the African coast.
This paper	Satellite	-39.6 ± 10.0 (Satellite)	
	Satellite+SBD	$-32.2 \sim -44.3$ (SBDART)	
	ART		
Li et al (2020)	Ground+SBD	$-45 \sim -50$	Instantaneous $DRFE_{dust}$.
	ART		
Xia and Zong (2009)	Satellite + SBDART	-48.1	Instantaneous $DRFE_{dust}$ at about 05:00 UTC.
This paper	Satellite	-48.6 ± 13.7 (Satellite)	
	Satellite+SBD	$-41.5 \sim -47.4$ (SBDART)	
	ART		

499

500 Table 2 illustrates the SW $DRFE_{dust}$ of the Sahara Desert and the Taklimakan Desert in previous
501 studies. Li et al. (2004) estimated the diurnal mean $DRFE_{dust}$ at the TOA ($-35 \pm 3 \text{ W m}^{-2} \tau^{-1}$ in summer;
502 $-26 \pm 3 \text{ W m}^{-2} \tau^{-1}$ in winter) over the Atlantic Ocean near the African coast. The results indicated that
503 lower uncertainties are derived from the standard deviation of the best-fit curve around the observed
504 points due to the binned mean fitting. For the Taklimakan Desert, Li et al. (2020) estimated the
505 instantaneous SW $DRFE_{dust}$ at the TOA of Kashi on April 2019. In this paper, the $DRFE_{dust}$ of the
506 Taklimakan Desert is estimated with the same dust properties referring to the works of Li et al. (2020).
507 Furthermore, Xia and Zong (2009) used both the satellite data and the SBDART model to represent the
508 instantaneous (about 05:00 UTC) SW $DRFE_{dust}$, which is $-48.1 \text{ W m}^{-2} \tau^{-1}$ at the TOA (Xia and Zong,
509 2009). Through comparison, it is found that the satellite-based equi-albedo method and the SBDART
510 model-derived SW $DRFE_{dust}$ are $-39.6 \pm 10.0 \text{ W m}^{-2} \tau^{-1}$ and -32.2 to $-44.3 \text{ W m}^{-2} \tau^{-1}$ at the TOA over
511 the Sahara Desert, respectively, which are $-48.6 \pm 13.7 \text{ W m}^{-2} \tau^{-1}$ and -41.5 to $-47.4 \text{ W m}^{-2} \tau^{-1}$ at the
512 TOA over the Taklimakan Desert, respectively. The methods and results in these studies are
513 comparable despite the differences. The results show that the negative $DRFE_{dust}$ from the Taklimakan
514 Desert is more significant than those from the Sahara Desert. As the SZA and LSA variations are
515 considered in these studies, the results in this paper are reasonable and reliable. The compared results
516 show that the $DRFE_{dust}$ derived from the satellite-based equi-albedo method is closer to that in previous

517 studies. The $DRFE_{\text{dust}}$ estimated by the satellite-based equi-albedo method is obtained without the dust
518 microphysical properties being assumed. The uncertainties are mostly caused by observation errors.
519 Therefore, the uncertainties can be estimated objectively. It provides a direct way to validate the
520 DRE_{dust} and the $DRFE_{\text{dust}}$.

521 **6 Discussion and conclusions**

522 This study analyzes the differences in the dust microphysical properties and the $DRFE_{\text{dust}}$ over the
523 Taklimakan Desert and the Sahara Desert during dust storms. The satellite-based equi-albedo method
524 and the RTM are both used to estimate the $DRFE_{\text{dust}}$ in this study. By comparing the results from
525 different methods and dust source regions, the $DRFE_{\text{dust}}$ differences caused by dust microphysical
526 properties and particle shapes are discussed.

527 The results show that the dust aerosols from the Taklimakan Desert around Kashi have higher
528 aerosol scattering (higher SSA) and backward scattering (lower ASY), and it causes more significant
529 negative $DRFE_{\text{dust}}$ ($-48.6 \pm 13.7 \text{ W m}^{-2} \tau^{-1}$ by the satellite; -41.5 to $-47.4 \text{ W m}^{-2} \tau^{-1}$ by the SBDART)
530 than that in the Sahara Desert around Tamanrasset ($-39.6 \pm 10.0 \text{ W m}^{-2} \tau^{-1}$ by the satellite; -32.2 to
531 $-44.3 \text{ W m}^{-2} \tau^{-1}$ by the SBDART). It is indicated that the dust microphysical properties and particle
532 shapes can significantly influence on the $DRFE_{\text{dust}}$. The information on the accurate dust microphysical
533 properties and dust origins is highly required in the $DRFE_{\text{dust}}$ simulation. The scant measurements on
534 dust microphysical properties can cause large uncertainties in simulating the $DRFE_{\text{dust}}$. Previous studies
535 proved that the results in this paper are reasonable and reliable. The $DRFE_{\text{dust}}$ derived from the
536 satellite-based equi-albedo method is close to the results in previous studies.

537 However, there are still uncertainties in the simulation of the $DRFE_{\text{dust}}$. In contrast, the $DRFE_{\text{dust}}$
538 can be estimated directly from the satellite observation using the equi-albedo method without any
539 assumptions of the microphysical properties of dust aerosols. It has unique advantages in estimating the
540 $DRFE_{\text{dust}}$. Also, it can validate the DRE_{dust} and the $DRFE_{\text{dust}}$ derived from the numerical models more
541 directly.

542 **Data availability**

543 The CERES data can be accessed from the Atmospheric Sciences Data Center of NASA Langley
544 Research Center (https://ceres.larc.nasa.gov/order_data.php). The AQUA/MODIS aerosol Products
545 (MYD04_L2) can be accessed from the NASA Level-1 and Atmosphere Archive and Distribution
546 System (LAADS) Distributed Active Archive Center (DAAC) website
547 (<https://ladsweb.modaps.eosdis.nasa.gov/>). The MODIS albedo products (MCD43C3 Version 6) can be
548 accessed from the NASA LP DAAC website (<https://lpdaac.usgs.gov/tools/data-pool/>). The
549 AERONET data were obtained from the AERONET website (<http://aeronet.gsfc.nasa.gov>).

550 **Author contributions**

551 PZ and LC designed the study, and LT performed the study with suggestions from PZ and LC. LB
552 improved the scattering calculating method of dust particles. Both authors contributed to the writing of
553 this article.

554 **Competing interests**

555 The authors declare that they have no conflict of interest.

556 **Special issue statement**

557 This article is part of the special issue “Satellite and ground-based remote sensing of aerosol
558 optical, physical, and chemical properties over China”. It is not associated with a conference.

559 **Acknowledgments**

560 We acknowledge the groups of MODIS, CERES, ECMWF, AERONET and GISS, for providing
561 the AOD, LSA, integrated water vapor, aerosol microphysical, optical properties products and T-matrix
562 code. We also thank the SBDART group for making SBDART available. We thank Nanjing Hurricane
563 Translation for reviewing the English language quality of this paper.

564 **Financial support**

565 This work was funded by the National Key R&D Program of China (grant number
566 2018YFB0504900 and 2018YFB0504905), National Natural Science Foundation (grant number
567 41675036).

568 **References**

569 Anderson, T. L., Charlson, R. J., Bellouin, N., Boucher, O., Chin, M., Christopher, S. A., Haywood, J.,
570 Kaufman, Y. J., Kinne, S., Ogren, J. A., Remer, L. A., Takemura, T., Tanré D., Torres, O., Trepte, C. R.,
571 Wielicki, B. A., Winker, D. M., and Yu, H.: An “A-Train” Strategy for Quantifying Direct Climate
572 Forcing by Anthropogenic Aerosols, *Bulletin of the American Meteorological Society*, 86, 1795-1810,
573 10.1175/bams-86-12-1795, 2005.

574 Bi, J., Shi, J., Xie, Y., Liu, Y., Takamura, T., and Khatri, P.: Dust Aerosol Characteristics and Shortwave
575 Radiative Impact at a Gobi Desert of Northwest China during the Spring of 2012, *Journal of the*
576 *Meteorological Society of Japan. Ser. II*, 92A, 33-56, 10.2151/jmsj.2014-A03, 2014.

577 Bi, L., Ding, S., Zong, R., and Yi, B.: Examining Asian dust refractive indices for brightness temperature
578 simulations in the 650–1135 cm⁻¹ spectral range, *Journal of Quantitative Spectroscopy and Radiative*
579 *Transfer*, 247, 106945, <https://doi.org/10.1016/j.jqsrt.2020.106945>, 2020.

580 Borghese, F., Denti, P., Saija, R., and Iatì M. A.: Optical trapping of nonspherical particles in the
581 T-matrix formalism, *Opt. Express*, 15, 11984-11998, 10.1364/OE.15.011984, 2007.

582 Che, H., Zhang, X., Alfraro, S., Chatenet, B., Gomes, L., and Zhao, J.: Aerosol optical properties and its
583 radiative forcing over Yulin, China in 2001 and 2002, *Advances in Atmospheric Sciences*, 26, 564-576,
584 10.1007/s00376-009-0564-4, 2009.

585 Che, H., Wang, Y., Sun, J., Zhang, X., Zhang, X., and Guo, J.: Variation of Aerosol Optical Properties
586 over Taklimakan Desert of China, *Aerosol and Air Quality Research*, 13, 777-785,
587 10.4209/aaqr.2012.07.0200, 2012.

588 Chen, L., Shi, G., Qin, S., Yang, S., and Zhang, P.: Direct radiative forcing of anthropogenic aerosols
589 over oceans from satellite observations, *Advances in Atmospheric Sciences*, 28, 973-984,
590 10.1007/s00376-010-9210-4, 2011.

591 Christopher, S. A., Chou, J., Zhang, J., Li, X., Berendes, T. A., and Welch, R. M.: Shortwave direct
592 radiative forcing of biomass burning aerosols estimated using VIRS and CERES data, *Geophysical*
593 *Research Letters*, 27, 2197-2200, 10.1029/1999gl010923, 2000.

594 Chylek, P., Grams, G., and Pinnick, R.: *Light Scattering by Nonspherical Particles*, 82, 1977.

595 Colarco, P. R., Nowotnick, E. P., Randles, C. A., Yi, B., Yang, P., Kim, K.-M., Smith, J. A., and
596 Bardeen, C. G.: Impact of radiatively interactive dust aerosols in the NASA GEOS-5 climate model:
597 Sensitivity to dust particle shape and refractive index, *Journal of Geophysical Research: Atmospheres*,
598 119, 753-786, 10.1002/2013jd020046, 2014.

599 Di Biagio, C., di Sarra, A., Eriksen, P., Ascanius, S. E., Muscari, G., and Holben, B.: Effect of surface
600 albedo, water vapour, and atmospheric aerosols on the cloud-free shortwave radiative budget in the
601 Arctic, *Climate Dynamics*, 39, 953-969, 10.1007/s00382-011-1280-1, 2012.

602 Di Biagio, C., Boucher, H., Caquineau, S., Chevaillier, S., Cuesta, J., and Formenti, P.: Variability of the
603 infrared complex refractive index of African mineral dust: Experimental estimation and implications for
604 radiative transfer and satellite remote sensing, *Atmospheric Chemistry and Physics*, 14,
605 10.5194/acp-14-11093-2014, 2014a.

606 Di Biagio, C., Formenti, P., Styler, S. A., Pangui, E., and Doussin, J.-F.: Laboratory chamber
607 measurements of the longwave extinction spectra and complex refractive indices of African and Asian
608 mineral dust, *Geophysical Research Letters*, 41, 10.1002/2014GL060213, 2014b.

609 Di Biagio, C., Formenti, P., Balkanski, Y., Caponi, L., Cazaunau, M., Pangui, E., Journet, E., Nowak, S.,
610 Caquineau, S., Andreae, M. O., Kandler, K., Saeed, T., Piketh, S., Seibert, D., Williams, E., and Doussin,
611 J. F.: Global scale variability of the mineral dust long-wave refractive index: a new dataset of in situ
612 measurements for climate modeling and remote sensing, *Atmos. Chem. Phys.*, 17, 1901-1929,
613 10.5194/acp-17-1901-2017, 2017.

614 Dubovik, O., and King, M. D.: A flexible inversion algorithm for retrieval of aerosol optical properties
615 from Sun and sky radiance measurements, *Journal of Geophysical Research: Atmospheres*, 105,
616 20673-20696, 10.1029/2000jd900282, 2000.

617 Dubovik, O., Sinyuk, A., Lapyonok, T., Holben, B. N., Mishchenko, M., Yang, P., Eck, T. F., Volten, H.,
618 Muñoz, O., Veihelmann, B., van der Zande, W. J., Leon, J.-F., Sorokin, M., and Slutsker, I.: Application
619 of spheroid models to account for aerosol particle nonsphericity in remote sensing of desert dust, *Journal*
620 *of Geophysical Research: Atmospheres*, 111, 10.1029/2005jd006619, 2006.

621 Gao, Y., and Anderson, J. R.: Characteristics of Chinese aerosols determined by individual-particle
622 analysis, *Journal of Geophysical Research: Atmospheres*, 106, 18037-18045, 10.1029/2000jd900725,
623 2001.

624 Garc ía, O. E., D íaz, A. M., Exp ósito, F. J., D íaz, J. P., Dubovik, O., Dubuisson, P., Roger, J.-C., Eck, T.
625 F., Sinyuk, A., Derimian, Y., Dutton, E. G., Schafer, J. S., Holben, B. N., and Garc ía, C. A.: Validation of
626 AERONET estimates of atmospheric solar fluxes and aerosol radiative forcing by ground-based
627 broadband measurements, *Journal of Geophysical Research: Atmospheres*, 113, 10.1029/2008jd010211,
628 2008.

629 Garc ía, O. E., D íaz, J. P., Exp ósito, F. J., D íaz, A. M., Dubovik, O., Derimian, Y., Dubuisson, P., and
630 Roger, J. C.: Shortwave radiative forcing and efficiency of key aerosol types using AERONET data,
631 *Atmos. Chem. Phys.*, 12, 5129-5145, 10.5194/acp-12-5129-2012, 2012.

632 Garrett, T. J., and Zhao, C.: Increased Arctic cloud longwave emissivity associated with pollution from
633 mid-latitudes, *Nature*, 440, 787-789, 10.1038/nature04636, 2006.

634 Gouesbet, G., and Gr éhan, G.: *Generalized Lorenz-Mie Theories*, 2011.

635 Guirado-Fuentes, C., Cuevas, E., Cachorro, V., Toledano, C., Alonso-P érez, S., Bustos, J., Basart, S.,
636 Romero, P., Camino, C., Mimouni, M., Zeudmi, L., Goloub, P., Baldasano, J., and Frutos Baraja, A.:
637 Aerosol characterization at the Saharan AERONET site Tamanrasset, *Atmospheric Chemistry and*
638 *Physics*, 14, 11753-11773, 10.5194/acp-14-11753-2014, 2014.

639 Holben, B. N., Eck, T. F., Slutsker, I., Tanré D., Buis, J. P., Setzer, A., Vermote, E., Reagan, J. A.,
640 Kaufman, Y. J., Nakajima, T., Lavenu, F., Jankowiak, I., and Smirnov, A.: AERONET—A Federated
641 Instrument Network and Data Archive for Aerosol Characterization, *Remote Sensing of Environment*,
642 66, 1-16, [https://doi.org/10.1016/S0034-4257\(98\)00031-5](https://doi.org/10.1016/S0034-4257(98)00031-5), 1998.

643 Hsu, N. C., Tsay, S. C., King, M. D., and Herman, J. R.: Aerosol properties over bright-reflecting source
644 regions, *IEEE Transactions on Geoscience & Remote Sensing*, 42, 557-569, 2004.

645 Huang, J., Fu, Q., Su, J., and Tang, Q.: Taklimakan dust aerosol radiative heating derived from
646 CALIPSO observations using the Fu-Liou radiation model with CERES constraints, *Atmospheric*
647 *Chemistry and Physics Discussions*, 2009.

648 Huang, J., Wang, T., Wang, W., Li, Z., and Yan, H.: Climate effects of dust aerosols over East Asian arid
649 and semiarid regions, *Journal of Geophysical Research: Atmospheres*, 119, 11,398-311,416,
650 10.1002/2014jd021796, 2014.

651 Huneeus, N., Chevallier, F., and Boucher, O.: Estimating aerosol emissions by assimilating observed
652 aerosol optical depth in a global aerosol model, *Atmospheric Chemistry & Physics*, 12, 4585-4606,
653 10.5194/acp-12-4585-2012, 2012.

654 Iftikhar, M., Alam, K., Sorooshian, A., Syed, W. A., Bibi, S., and Bibi, H.: Contrasting aerosol optical
655 and radiative properties between dust and urban haze episodes in megacities of Pakistan, *Atmospheric*
656 *Environment*, 173, 157-172, <https://doi.org/10.1016/j.atmosenv.2017.11.011>, 2018.

657 Jin, Y., Schaaf, C. B., Woodcock, C. E., Gao, F., Li, X., Strahler, A. H., Lucht, W., and Liang, S.:
658 Consistency of MODIS surface bidirectional reflectance distribution function and albedo retrievals: 2.
659 Validation, *Journal of Geophysical Research: Atmospheres*, 108, 10.1029/2002jd002804, 2003.

660 Kalashnikova, O. V., and Sokolik, I. N.: Modeling the radiative properties of nonspherical soil-derived
661 mineral aerosols, *Journal of Quantitative Spectroscopy and Radiative Transfer*, 87, 137-166,
662 <https://doi.org/10.1016/j.jqsrt.2003.12.026>, 2004.

663 Lewis, P., and Barnsley, M.: Influence of the sky radiance distribution on various formulations of the
664 Earth surface albedo, *Proc. Conf. Phys. Meas. Sign. Remote Sens.*, 1994.

665 Li, F., Vogelmann, A. M., and Ramanathan, V.: Saharan Dust Aerosol Radiative Forcing Measured from
666 Space, *Journal of Climate*, 17, 2558-2571, 10.1175/1520-0442(2004)017<2558:SDARFM>2.0.CO;2,
667 2004.

668 Li, L., Li, Z., Chang, W., Ou, Y., Goloub, P., Li, C., Li, K., Hu, Q., Wang, J., and Wendisch, M.: Solar
669 radiative forcing of aerosol particles near the Taklimakan desert during the Dust Aerosol
670 Observation-Kashi campaign in Spring 2019, *Atmos. Chem. Phys. Discuss.*, 2020, 1-29,
671 10.5194/acp-2020-60, 2020.

672 Li, Z. Q., Xu, H., Li, K. T., Li, D. H., Xie, Y. S., Li, L., Zhang, Y., Gu, X. F., Zhao, W., Tian, Q. J., Deng,
673 R. R., Su, X. L., Huang, B., Qiao, Y. L., Cui, W. Y., Hu, Y., Gong, C. L., Wang, Y. Q., Wang, X. F.,
674 Wang, J. P., Du, W. B., Pan, Z. Q., Li, Z. Z., and Bu, D.: Comprehensive Study of Optical, Physical,
675 Chemical, and Radiative Properties of Total Columnar Atmospheric Aerosols over China: An Overview
676 of Sun-Sky Radiometer Observation Network (SONET) Measurements, *Bulletin of the American*
677 *Meteorological Society*, 99, 739-755, 10.1175/bams-d-17-0133.1, 2018.

678 Liang, S., Fang, H., Chen, M., Shuey, C. J., Walthall, C., Daughtry, C., Morisette, J., Schaaf, C., and
679 Strahler, A.: Validating MODIS land surface reflectance and albedo products: methods and preliminary

680 results, *Remote Sensing of Environment*, 83, 149-162, [https://doi.org/10.1016/S0034-4257\(02\)00092-5](https://doi.org/10.1016/S0034-4257(02)00092-5),
681 2002.

682 Liu, J., Schaaf, C., Strahler, A., Jiao, Z., Shuai, Y., Zhang, Q., Roman, M., Augustine, J. A., and Dutton,
683 E. G.: Validation of Moderate Resolution Imaging Spectroradiometer (MODIS) albedo retrieval
684 algorithm: Dependence of albedo on solar zenith angle, *Journal of Geophysical Research: Atmospheres*,
685 114, 10.1029/2008jd009969, 2009.

686 Mbourou, G. N. T., Bertrand, J. J., and Nicholson, S. E.: The Diurnal and Seasonal Cycles of
687 Wind-Borne Dust over Africa North of the Equator, *Journal of Applied Meteorology*, 36, 868-882,
688 10.1175/1520-0450(1997)036<0868:Tdasco>2.0.Co;2, 1997.

689 McComiskey, A., Ricchiazzi, P., Ogren, J., and Dutton, E.: SGPGET: AN SBDART Module for Aerosol
690 Radiative Transfer, 2021.

691 Mikami, M., Shi, G. Y., Uno, I., Yabuki, S., Iwasaka, Y., Yasui, M., Aoki, T., Tanaka, T. Y., Kurosaki,
692 Y., Masuda, K., Uchiyama, A., Matsuki, A., Sakai, T., Takemi, T., Nakawo, M., Seino, N., Ishizuka, M.,
693 Satake, S., Fujita, K., Hara, Y., Kai, K., Kanayama, S., Hayashi, M., Du, M., Kanai, Y., Yamada, Y.,
694 Zhang, X. Y., Shen, Z., Zhou, H., Abe, O., Nagai, T., Tsutsumi, Y., Chiba, M., and Suzuki, J.: Aeolian
695 dust experiment on climate impact: An overview of Japan–China joint project ADEC, *Global and
696 Planetary Change*, 52, 142-172, <https://doi.org/10.1016/j.gloplacha.2006.03.001>, 2006.

697 Miller, R., Knippertz, P., Pérez García-Pando, C., Perlwitz, J., and Tegen, I.: Impact of Dust Radiative
698 Forcing upon Climate, in, 327-357, 2014.

699 Mishchenko, M. I., Travis, L. D., and Mackowski, D. W.: T-matrix computations of light scattering by
700 nonspherical particles: A review, *Journal of Quantitative Spectroscopy and Radiative Transfer*, 55,
701 535-575, [https://doi.org/10.1016/0022-4073\(96\)00002-7](https://doi.org/10.1016/0022-4073(96)00002-7), 1996.

702 Mishchenko, M. I., and Travis, L. D.: Capabilities and limitations of a current FORTRAN
703 implementation of the T-matrix method for randomly oriented, rotationally symmetric scatterers, *Journal
704 of Quantitative Spectroscopy and Radiative Transfer*, 60, 309-324,
705 [https://doi.org/10.1016/S0022-4073\(98\)00008-9](https://doi.org/10.1016/S0022-4073(98)00008-9), 1998.

706 Mishchenko, M. I., and Travis, L. D.: Gustav Mie and the Evolving Discipline of Electromagnetic
707 Scattering by Particles, *Bulletin of the American Meteorological Society*, 89, 1853-1862,
708 10.1175/2008bams2632.1, 2008.

709 Nakajima, T., Tanaka, M., Yamano, M., Shiobara, M., Arao, K., and Nakanishi, Y.: Aerosol Optical
710 Characteristics in the Yellow Sand Events Observed in May, 1982 at Nagasaki-Part II Models, Journal of
711 the Meteorological Society of Japan. Ser. II, 67, 279-291, 10.2151/jmsj1965.67.2_279, 1989.

712 Okada, K., Heintzenberg, J., Kai, K., and Qin, Y.: Shape of atmospheric mineral particles collected in
713 three Chinese arid-regions, Geophysical Research Letters, 28, 3123-3126, 10.1029/2000gl012798, 2001.

714 Qie, L., Li, L., Li, K., Li, D., and Xu, H.: Retrieval of aerosol optical properties from ground-based
715 remote sensing measurements: Aerosol asymmetry factor and single scattering albedo, 2019.

716 Ramanathan, V., Cess, R., Harrison, E., Minnis, P., Barkstrom, B., Ahmad, E., and Hartmann, D.:
717 Cloud-Radiative Forcing and Climate: Results from The Earth Radiation Budget Experiment, Science
718 (New York, N.Y.), 243, 57-63, 10.1126/science.243.4887.57, 1989.

719 Remer, L. A., Kaufman, Y. J., Tanré D., Mattoo, S., Chu, D. A., Martins, J. V., Li, R. R., Ichoku, C.,
720 Levy, R. C., Kleidman, R. G., Eck, T. F., Vermote, E., and Holben, B. N.: The MODIS Aerosol
721 Algorithm, Products, and Validation, Journal of the Atmospheric Sciences, 62, 947-973,
722 10.1175/JAS3385.1, 2005.

723 Ricchiazzi, P., Yang, S., Gautier, C., and Soble, D.: SBDART: A Research and Teaching Software Tool
724 for Plane-Parallel Radiative Transfer in the Earth's Atmosphere, Bulletin of the American
725 Meteorological Society, 79, 2101-2114, 10.1175/1520-0477(1998)079<2101:Satrats>2.0.Co;2, 1998a.

726 Ricchiazzi, P., Yang, S., Gautier, C., and Soble, D.: SBDART: A Research and Teaching Software Tool
727 for Plane-Parallel Radiative Transfer in the Earth's Atmosphere, Bulletin of the American
728 Meteorological Society, 79, 2101, 10.1175/1520-0477(1998)079<2101:Satrats>2.0.Co;2, 1998b.

729 Román, M. O., Schaaf, C. B., Lewis, P., Gao, F., Anderson, G. P., Privette, J. L., Strahler, A. H.,
730 Woodcock, C. E., and Barnsley, M.: Assessing the coupling between surface albedo derived from
731 MODIS and the fraction of diffuse skylight over spatially-characterized landscapes, Remote Sensing of
732 Environment, 114, 738-760, <https://doi.org/10.1016/j.rse.2009.11.014>, 2010.

733 Satheesh, S. K., and Ramanathan, V.: Large differences in tropical aerosol forcing at the top of the
734 atmosphere and Earth's surface, Nature, 405, 60-63, 10.1038/35011039, 2000.

735 Satheesh, S. K.: *Letter to the Editor*
736 Aerosol radiative forcing over land: effect of surface
737 and cloud reflection, Ann. Geophys., 20, 2105-2109, 10.5194/angeo-20-2105-2002, 2002.

737 Satheesh, S. K., and Srinivasan, J.: A Method to Estimate Aerosol Radiative Forcing from Spectral
738 Optical Depths, Journal of Atmospheric Sciences, 63, 1082, 10.1175/jas3663.1, 2006.

739 Sayer, A. M., Munchak, L. A., Hsu, N. C., Levy, R. C., Bettenhausen, C., and Jeong, M.-J.: MODIS
740 Collection 6 aerosol products: Comparison between Aqua's e-Deep Blue, Dark Target, and “merged”
741 data sets, and usage recommendations, *Journal of Geophysical Research: Atmospheres*, 119,
742 13,965-913,989, 10.1002/2014jd022453, 2014.

743 Schaaf, C., Martonchik, J., Pinty, B., Govaerts, Y., Gao, F., Lattanzio, A., Liu, J., Strahler, A., and
744 Taberner, M.: Retrieval of Surface Albedo from Satellite Sensors, in: *Advances in Land Remote Sensing:
745 System, Modeling, Inversion and Application*, edited by: Liang, S., Springer Netherlands, Dordrecht,
746 219-243, 2008.

747 Schaaf, C. B., Gao, F., Strahler, A. H., Lucht, W., Li, X., Tsang, T., Strugnell, N. C., Zhang, X., Jin, Y.,
748 Muller, J.-P., Lewis, P., Barnsley, M., Hobson, P., Disney, M., Roberts, G., Dunderdale, M., Doll, C.,
749 d'Entremont, R. P., Hu, B., Liang, S., Privette, J. L., and Roy, D.: First operational BRDF, albedo nadir
750 reflectance products from MODIS, *Remote Sensing of Environment*, 83, 135-148,
751 [https://doi.org/10.1016/S0034-4257\(02\)00091-3](https://doi.org/10.1016/S0034-4257(02)00091-3), 2002a.

752 Schaaf, C. B., Gao, F., Strahler, A. H., Lucht, W., Li, X., Tsang, T., Strugnell, N. C., Zhang, X., Jin, Y.,
753 Muller, J.-P., Lewis, P., Barnsley, M., Hobson, P., Disney, M., Roberts, G., Dunderdale, M., Doll, C.,
754 d'Entremont, R. P., Hu, B., Liang, S., Privette, J. L., and Roy, D.: First operational BRDF, albedo nadir
755 reflectance products from MODIS, *Remote Sensing of Environment*, 83, 135,
756 10.1016/s0034-4257(02)00091-3, 2002b.

757 Schaaf, C. B., Liu, J., Gao, F., and Strahler, A. H.: Aqua and Terra MODIS Albedo and Reflectance
758 Anisotropy Products, in: *Land Remote Sensing and Global Environmental Change: NASA's Earth
759 Observing System and the Science of ASTER and MODIS*, edited by: Ramachandran, B., Justice, C. O.,
760 and Abrams, M. J., Springer New York, New York, NY, 549-561, 2011.

761 Shi, G., Wang, H., Wang, B., Li, W., Gong, S., Zhao, T., and Aoki, T.: Sensitivity Experiments on the
762 Effects of Optical Properties of Dust Aerosols on Their Radiative Forcing under Clear Sky Condition,
763 *Journal of The Meteorological Society of Japan - J METEOROL SOC JPN*, 83A, 333-346,
764 10.2151/jmsj.83A.333, 2005.

765 Slingo, A., Ackerman, T. P., Allan, R. P., Kassianov, E. I., McFarlane, S. A., Robinson, G. J., Barnard, J.
766 C., Miller, M. A., Harries, J. E., Russell, J. E., and Dewitte, S.: Observations of the impact of a major
767 Saharan dust storm on the atmospheric radiation balance, *Geophysical Research Letters*, 33,
768 10.1029/2006gl027869, 2006.

769 Tanré D., Kaufman, Y., Holben, B., Chatenet, B., Karnieli, A., Lavenu, F., Blarel, L., Dubovik, O.,
770 Remer, L., and Smirnov, A.: Climatology of dust aerosol size distribution and optical properties derived
771 from remotely sensed data in the solar spectrum, *Journal of Geophysical Research*, 106,
772 10.1029/2000JD900663, 2001.

773 Tegen, I., Bierwirth, E., Heinold, B., Helmert, J., and Wendisch, M.: Effect of measured surface albedo
774 on modeled Saharan dust solar radiative forcing, *Journal of Geophysical Research: Atmospheres*, 115,
775 10.1029/2009jd013764, 2010.

776 Textor, C., Schulz, M., Guibert, S., Kinne, S., Balkanski, Y., Bauer, S., Bernsten, T., Berglen, T.,
777 Boucher, O., Chin, M., Dentener, F., Diehl, T., Feichter, J., Fillmore, D., Ginoux, P., Gong, S., Grini, A.,
778 Hendricks, J., Horowitz, L., Huang, P., Isaksen, I. S. A., Iversen, T., Kloster, S., Koch, D., Kirkevåg, A.,
779 Kristjansson, J. E., Krol, M., Lauer, A., Lamarque, J. F., Liu, X., Montanaro, V., Myhre, G., Penner, J. E.,
780 Pitari, G., Reddy, M. S., Seland, Ø., Stier, P., Takemura, T., and Tie, X.: The effect of harmonized
781 emissions on aerosol properties in global models – an AeroCom experiment, *Atmos. Chem. Phys.*, 7,
782 4489-4501, 10.5194/acp-7-4489-2007, 2007.

783 Tian, L., Zhang, P., and Chen, L.: Estimation of the Dust Aerosol Shortwave Direct Forcing Over Land
784 Based on an Equi-albedo Method From Satellite Measurements, *Journal of Geophysical Research:*
785 *Atmospheres*, 124, 8793-8807, 10.1029/2019JD030974, 2019.

786 Valenzuela, A., Olmo, F. J., Lyamani, H., Antón, M., Quirantes, A., and Alados-Arboledas, L.: Aerosol
787 radiative forcing during African desert dust events (2005–2010) over Southeastern Spain, *Atmospheric*
788 *Chemistry and Physics (ACP) & Discussions (ACPD)*, 2012.

789 Wang, Z., Zhang, H., Jing, X., and Wei, X.: Effect of non-spherical dust aerosol on its direct radiative
790 forcing, *Atmospheric Research*, 120-121, 112-126, <https://doi.org/10.1016/j.atmosres.2012.08.006>,
791 2013.

792 Wielicki, B. A., Barkstrom, B. R., Baum, B. A., Charlock, T. P., Green, R. N., Kratz, D. P., Lee, R. B.,
793 Minnis, P., Smith, G. L., Takmeng, W., Young, D. F., Cess, R. D., Coakley, J. A., Crommelynck, D. A.
794 H., Donner, L., Kandel, R., King, M. D., Miller, A. J., Ramanathan, V., Randall, D. A., Stowe, L. L., and
795 Welch, R. M.: Clouds and the Earth's Radiant Energy System (CERES): algorithm overview, *IEEE*
796 *Transactions on Geoscience and Remote Sensing*, 36, 1127-1141, 1998.

797 Xia, X., and Zong, X.: Shortwave versus longwave direct radiative forcing by Taklimakan dust aerosols,
798 *Geophysical Research Letters*, 36, 10.1029/2009gl037237, 2009.

799 Zhang, J., Christopher, S. A., Remer, L. A., and Kaufman, Y. J.: Shortwave aerosol radiative forcing
800 over cloud-free oceans from Terra: 2. Seasonal and global distributions, *Journal of Geophysical*
801 *Research (Atmospheres)*, 110, D10S24, 2005.

802 Zhang, P., Lu, N.-m., Hu, X.-q., and Dong, C.-h.: Identification and physical retrieval of dust storm using
803 three MODIS thermal IR channels, *Global and Planetary Change*, 52, 197-206,
804 <https://doi.org/10.1016/j.gloplacha.2006.02.014>, 2006.

805 Zhao, C., Chen, S., Leung, L. R., Qian, Y., Kok, J. F., Zaveri, R. A., and Huang, J.: Uncertainty in
806 modeling dust mass balance and radiative forcing from size parameterization, *Atmos. Chem. Phys.*, 13,
807 10733-10753, 10.5194/acp-13-10733-2013, 2013.

808